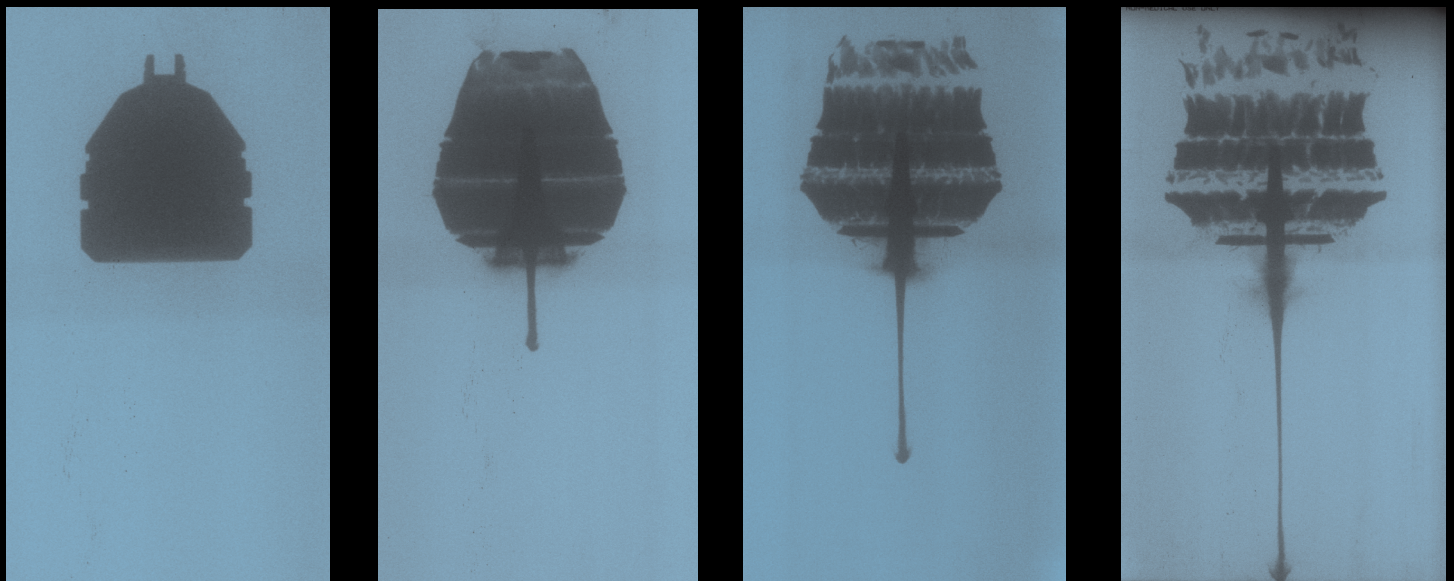


# Journal International Perforating Forum

VOL.2, ISSUE NO.1/JULY 2018

A Journal For The International Perforating Industry



Cover Illustration by Halliburton

**ARTICLE 1.** A Technique for Dynamic Evaluation of Perforator Performance

**ARTICLE 2.** Analyzing API RP 19B, Section 4 Perforation Flow Testing Data – Part 1

**ARTICLE 3.** Product Certification Testing of Perforating System Components

ISSN 2471-9374

# INSIDE

- 3** MESSAGE FROM THE IPFC BOARD OF DIRECTORS
- 4** EDITORS' MESSAGE
- 5** CONTINUING EDUCATION. YOUNG PROFESSIONALS
- 6** SAFETY
- 7** NEWS
- 8** REGIONAL UPDATES

**12** ARTICLE 1. A Technique for Dynamic Evaluation of Perforator Performance

**22** ARTICLE 2. Analyzing API RP 19B, Section 4 Perforation Flow Testing Data – Part 1

**60**

ARTICLE 3. Product Certification Testing of Perforating System Components

# MESSAGE FROM THE IPFC BOARD OF DIRECTORS



**James Barker**



**Mark Brinden**



**John JW Segura**

2018 started off busy for the International Perforating Forum (IPF) and it is a reflection of the increased activity in our industry. The Asia Pacific Perforating Symposium (APPS) was held in March with solid attendance and a full suite of presentations. And upcoming in the next few days will be the North America Perforating Symposium (NAPS) to be held in Galveston, Texas. Already the registration rolls show this will be a highly-attended and broadly-sponsored event. There were many good abstract submissions to NAPS, to the point where the presentation agenda and poster session quickly became full, thus leaving several good abstracts as candidates for the next symposiums. The IPF Board of Directors encourages those authors to continue submitting these works to future symposiums!

The Board further recognizes that events like APPS and NAPS do not happen on their own – they require big efforts with many volunteers who expend substantial personal time. We extend our sincere thanks to these tireless individuals who make these events successful.

The Board of Directors is also glad to report that the IPF organization continues to grow stronger and stronger. Our non-profit organization recently amended the bylaws to provide a clearer path for adding new Directors and voting protocols. Most recently David Ayre was added as fourth Director of the IPF and was

also named as Vice-President (Welcome David!). Each year at the annual meeting of the IPF, nominations and voting are held to establish the upcoming year's Directors and Officers positions. The next annual meeting will be held during the 2018 NAPS event and we encourage the IPF volunteers to be part of the nomination and voting process.

Finally, the Board of Directors recognizes the dedicated work by the JIPF editors and peer-review industry experts who contribute their time to review the article submissions. This process ensures that the technical quality of the Journal remains high and relevant to the current state of our perforating industry. We believe you will find the articles for this 3rd edition of JIPF meet those criteria and we hope you enjoy reading them and absorbing their technical content. Thank you authors, editors, and peer-reviewers!

On behalf of the Directors of the IPFC  
 James Barker  
 Secretary, IPFC

# EDITORS' MESSAGE

Welcome to the third issue of the Journal of the International Perforating Forum. This issue follows an extremely busy year within the industry. Although the industry is recovering to some extent from the biggest downturn in at least a generation, the pressure to do more with less is not going away. The landscape remains marked by continual changes in both people and technology, as the industry continually evolves in its quest to obtain more barrels at lower cost, minimizing risk while keeping safety paramount.



**John Carminati**



**Brenden Grove**

The Journal is pleased to feature 3 technical articles in this issue, an increase over earlier issues. All 3 articles relate to perforation testing, an interesting compliment to the modeling theme of the previous issue. Often a useful companion to modeling – or in cases where modeling may be lacking – laboratory testing can be useful to confirm performance and mitigate risk before field deployment. This is especially true in the realm of perforating, where confidence in downhole performance is essential to justify the significant investments involved.

As an organization, the IPF is in the midst of a busy 2018; among other things organizing 3 key symposia – focusing on the AsiaPacific, North America, and Latin America regions. AAPS was held in Kuala Lumpur in March. NAPS is being planned for Galveston in July/Aug, as the 10th anniversary of the inaugural IPS. SLAP is currently scheduled for Bogota in October. We are pleased to highlight these 3 events on the following pages.

As mentioned above, personnel changes are as constant as technology changes. In this spirit, we continue to invite and encourage increased participation – especially from newer entrants to the perforating community. This Journal, the regional and international symposia, and the IPF at large continue as vehicles to advance well perforation technology. The more community members put into these initiatives, the more the industry benefits.

As always, we sincerely thank all who made this issue possible. In addition to the content providers named throughout, this Journal would not be possible without the commitment exhibited by the technical editors, reviewers, and the organizations that support them.

John Carminati and Brenden Grove  
Executive Editors, JIPF

# CONTINUING EDUCATION

Welcome to the Continuing Education section. Please visit our website (<https://perforators.org/continuing-education/>) if you have not done it yet! We have included some technical publications on perforating we hope you will find interesting.

There is also a list of Perforating SPE/OTC papers archived under the same sections of IPF technical workshops, to simplify your search in OnePetro. We have invited colleagues from many companies to keep growing the list with their recommended papers.

Please let us know what other needs you think we should address under Continuing Education, by emailing [ajfayard@gmail.com](mailto:ajfayard@gmail.com)

Alfredo Fayard,  
Continuing Education Chair, IPF



//////  
**Alfredo Fayard**

# YOUNG PROFESSIONALS

In 2016 the IPFC began a Young Professionals group for members within the perforating industry. This recent downturn has proven that the need to maintain a high level of experience in our industry is critical. One of the ways to maintain this is by developing our younger generation of employees and enabling them to connect and learn from previous and experienced generations. Our industry is a "boom or bust" one and we need to make sure there is a future that is capable of supporting our industry, even in the bust.

The YP group would like to invite all individuals under the age of 35 to join and participate. The organization is focused on not only connecting current YP to senior members in our industry, but also as a link between the next generation of individuals and our community. This will include social gatherings, university outreach, and continuing education. It is the desire of the group to dedicate time and resources at future conferences to connecting the YP to the industry.

Our YP group is still just beginning and we have quite a bit to still work out. The benefit to the group is we are looking to reach out and connect with other YP to make this a group that truly fits our needs. We need to know what the YP community needs and wants, so we know how to focus our efforts. We highly encourage any interested to join in and participate and make this successful. We cannot do it without other YP and those who are able to mentor and provide valuable experience. Please send us an email at [yp@perforators.org](mailto:yp@perforators.org) if you are interested.

S. Geerts & C. Sokolove,  
YP Chairs, IPF



//////  
**Shaun Geerts**

SAFETY. 

# SAFETY

Safety is at the core of IPF's mission. This is applicable to explosives used in oil and gas producing operations, and more specifically to the use of explosives inside a wellbore. The IPF Safety Chair's goal is to collect and review incidents and near miss reports related to explosives and associated equipment used in oil and gas producing operations and to publish these. The purpose is to help the perforating industry to prevent inadvertent and unintentional detonation of explosives, help minimize risks and reduce explosive accidents to zero. In order to achieve this it is necessary for everybody to report any and all perforating related incidents and near misses to the safety data base on the PERFORATORS.ORG website. Only when collecting a wide range of incidents will we all be able to learn and make our environment a safer work place.



**Frank Preiss**

Remember to submit perforating related incidents and near misses  
In case of any questions please contact [frank.preiss@perforators.org](mailto:frank.preiss@perforators.org)

Frank Preiss,  
Safety Chairman, IPF

# NEWS

# Update



## Proposed API-19PT (Downhole Perforating Tools and Related Equipment)

As an outcome of the API-19B Task Group regular meeting on May 2, 2018 a new proposal for an industry standard that would provide specification for Downhole Perforating Tools and related equipment was born. The new standard was formally presented to the API 19 Subcommittee. This standard would define the minimum requirements for reporting and validating operational ratings of downhole perforating tools that are not addressed by any current standards or specifications. Downhole perforating tools are defined as all assemblies, components, and parts that are used to convey, actuate, retain, anchor, and release the perforating tool string.

The intention of the new standard is to close the gap within our industry addressing concerns related to downhole perforating tools that are not currently addressed by any other industry standard. This would provide servicing and operations standard quality assurances and defined functionality ratings (i.e. Operational and functionality ratings, traceability of materials, compatibility of tools between manufacturers). The proposal has been recommended for review by the Committee on Standardization of Oilfield Equipment & Materials (CSOEM) scheduled for August 1, 2018.

Chris Hoelscher



## API Thermal Decomposition Study of HMX

For some time, there has been concern with the limited information available regarding extended time exposure to temperature for HMX. Most readers will be familiar with the current industry charts, which provide guidelines regarding usage of various explosives following time and temperature exposure. However the data being used are far from comprehensive; thus it was recognized by the API RP19B committee as an urgent need to obtain more complete data. After some years of effort, we now have funding from API over the next 2 years to carry out extended testing of HMX. Lawrence Livermore National Laboratory, (LLNL) has agreed to take on the workscope and will carry out a number of tests, based on available funding to characterize the Time and Temperature to Ignition for HMX.

They will be using the 'One Dimensional Time to Explosion' (ODTX) system to run the tests. The test fixture can precisely measure times to explosion and minimum ignition temperatures of the HMX. The apparatus isothermally heats a 1.27 cm sample in a cavity between two aluminum anvils (see Figure 1). A piston drives the top and bottom heater and anvil downward together with a copper O ring providing a gas tight seal. Thermal ignition is indicated by the use of a microphone.

Testing is expected to take place over the next 18 months; it is hoped that the initial results will be available early in 2019. We plan to write up the results and submit for JIPF publication consideration as soon as the final results are in. Upon program completion, results will be made available via the API to the industry as a whole. The project is currently being run by Chris Sokolove and myself, and we hope to support the project to completion. Please address us both if you have any questions or wish to have some involvement in the project.

Mark S Brinsden

Chair, API RP19b Committee  
President, IPF  
Fellow, Energy Institute.

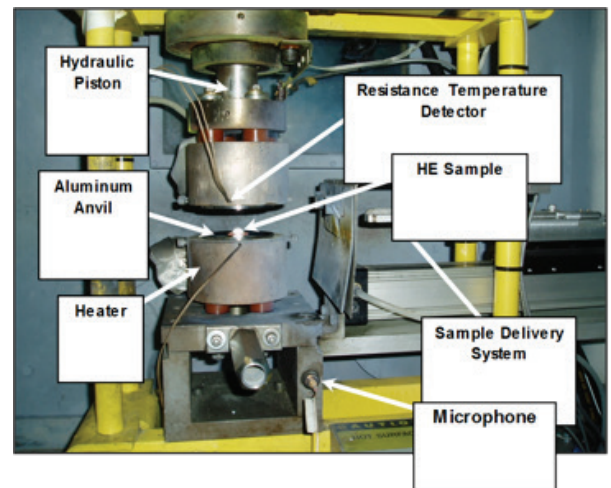


Figure 1. ODTX apparatus with key components labeled. (Courtesy of LLNL)



# REGIONAL UPDATES

# NORTH AMERICA

The North America Perforating Symposium will be held at Moody Gardens in Galveston, TX starting on July 31st. This two day symposium marks our tenth anniversary!

Richard Spears and David Otte will be the guest speakers. There will be 27 technical presentations on topics such as multi-stage completions, perforating dynamics and novel perforating concepts to name a few. A full list of topics, presentations and posters can be found on the Perforators.org website.

Registrations are still being accepted so don't miss out on this high quality technical program. We are grateful to the 30 companies which have sponsored this symposium.

[John Carminati- Shell](#)  
[Alphie Wright-Hunting Titan](#)  
NAPS 2018 Co-Chairs

# LATIN AMERICA

SLAP 2018 is on the way. From October 24th till 26th, the symposium will be held in Bogota, Colombia at the AR Convention Center. A large quantity of key people from Operators, Services Companies and this year also from the Colombian National Hydrocarbons Agency, are working as part of the Organization Committee. The Symposium will have the typical structure with two days of presentations mainly focused on the regional experiences and needs but with a global view on new technologies. As with previous SLAP events, presentations will be available in both Spanish and English, and delivered with translators.

Please visit [perforators.org](http://perforators.org) for more event information. Sponsoring opportunities are still available. Abstracts submission is open till August 24th. And registration will be open soon.

Hope to see you here,

[Fernando Armirola – CEPSA,](#)  
[Diana Chaparro – ECOPETROL](#)  
SLAP 2018 Co-Chairs

# ASIA PACIFIC

After several years of reduced drilling, completion, and intervention activity within the Asia Pacific Region, the record low activity seems to be slowly rebounding. With new developments being announced and project expansions being scoped and tendered, late 2018 and beyond appears promising for perforating activity.

We are also happy to report that in Q1 2018, after a several year delay, we were able to hold the latest Asia Pacific Perforating Symposium (APPS) in Kuala Lumpur, Malaysia. This well attended event hosted over 110 delegates representing 43 companies across 18 different countries; with Mr. Wan A Aziz Wan Razil, Head of Production Technology for Petronas Malaysia Petroleum Management (MPM) providing an insightful opening speech covering the key production challenges facing Malaysia. The caliber of material covered during the day and a half event, the quality of discussion, and participation of attendees demonstrated we are achieving the mission of IPF within Asia Pacific. This would not have been possible without the dedication of the full APPS committee and the support of our generous sponsors. We encourage you to review these excellent presentations <https://perforators.org/ips-presentations/>

If you would like to participate and volunteer on the next APPS Committee, please contact us.

[Clint Quattlebaum & John Davidson](#)



# RUSSIA

The Russia International Perforating Symposium (RIPS) was held during October 23-25, 2017, in Tyumen Russia. Further information can be found at [perforators.org](http://perforators.org).

# EUROPE

The last IPS Europe event was successfully held in May 2015 in Amsterdam. IPS Europe needs your support. Please step forward and volunteer to chair this event. Please contact one of the IPFC officers. Their contact details can be found on [perforators.org](http://perforators.org).

IPS EUROPE

# A Technique for Dynamic Evaluation of Perforator Performance

**Dennis W. Baum**, Lawrence Livermore National Laboratory  
**Mark Brinsden**, IPF, Shell International Petroleum Co. Ltd.

## SUMMARY

A radiographic methodology is presented which can measure the relative penetration efficiencies of different portions of a perforator jet. This knowledge can quantify the penetration efficiency of individual portions of a jet into specific target materials and thus identify design opportunities for improvement in perforator charge performance. The test methodology is a modification of a test configuration previously developed to characterize the erosion of a shaped charge jet when penetrating different thicknesses of drilling mud [1]. By replacing the drilling mud with concrete or other target materials of interest, perforator jet erosion rates can be directly measured as a function of discrete target thicknesses. The test configuration and data obtained from the drilling mud tests are described to illustrate the output attainable from the test configuration, followed by a discussion of the technique adapted to quantify perforator effectiveness in specific target materials of interest.

## INTRODUCTION

A test configuration was developed for quantifying the erosion of copper shaped charge jets penetrating drilling mud, in support of work for Shell International Exploration and Production Inc. The technique used radiography to simultaneously observe the decrease in jet lengths when multiple charges perforate targets of increasing thickness. A well characterized shaped charge was fired through drilling mud, a less understood target material and the jet erosion was measured as a function of mud thickness penetrated. We propose that the same test configuration can be used to observe the reverse situation of perforator jet erosion as a function of penetration depth into a known target material such as concrete. For example, the erosion data could provide understanding of the relative penetration efficiencies of the leading and trailing portions of a perforator jet, thereby providing opportunities for design of improved performance jets. While this paper describes in some detail the configuration developed to accurately measure copper jet loss resulting from penetration of different thicknesses of drilling mud, the technique is equally applicable to the study of the efficiency of granular perforator jets penetrating through concrete or geological materials. Note also that the test configuration provides a well-defined geometry which is useful in comparing observed jet loss with full physics simulations of jet loss.

---

## BACKGROUND

**Emergency Severance Tool (EST).** Lawrence Livermore National Laboratory (LLNL) performed work for Shell International Exploration and Production Inc. to provide an EST capability for severing various types of marine riser systems used in deep-sea drilling operations. The purpose of the EST is to rapidly release the surface drilling rig from the blowout preventer located on the seabed, in the event of a blowout scenario as occurred in the Macondo Gulf of Mexico event. The current design of the EST uses an array of copper linear shaped charges (LSCs) surrounding the marine riser system and designed to sever the marine riser and the enclosed steel drill string, providing immediate separation from the surface drilling rig. As the shaped charge jets are required to pass through an annulus of air, steel, and drilling mud before reaching the heavy walled drill string, the erosion of the jets passing through these media must be assessed. While the erosion of jets penetrating air and steel is well understood, the effect of drilling mud on jet propagation has not been characterized. In general, the shaped charge jet will be required to penetrate from 0 to 250mm of drilling mud before arriving at its target. To successfully achieve the severance goal, a substantial portion of the jet must remain intact after passing through the mud to penetrate into the drill collar. Thus, a combined experimental and simulation effort was created to characterize the erosion of shaped charge jets penetrating drilling mud.

**Shaped Charge.** To focus this study on the drilling mud, it was desired that the shaped charges used for this experiment used the same liner material (copper) as in the EST and be well understood and reproducible. Therefore, rather than using the LSCs (which were still in development), the 65mm Viper conical shaped charge was chosen for these tests. The precise design and reproducible behavior of these shaped charges makes them ideally suited for experimental investigations. Prior work [2] compared detailed jet formation simulations with experimental measurements of liner collapse and jet formation and verified our understanding of jet formation and propagation of a Viper jet.

## DESIGN OF EXPERIMENT

**Shot Configuration.** The experimental setup included a vertical array of three Viper shaped charges detonated simultaneously. **Fig. 1** shows a schematic representation of the experimental setup. The top charge is the control jet and passes through a 60mm empty polycarbonate tank. The middle charge passes through a 60mm mud-filled tank, while the bottom charge passes through a 120mm mud-filled tank. Side-on x-ray images were used to capture the jet tip positions before and after passing through the tanks to confirm simultaneity and visualize the resulting jet erosion. Two identical experiments in this configuration were performed, designated Mud Test A and Mud Test B.

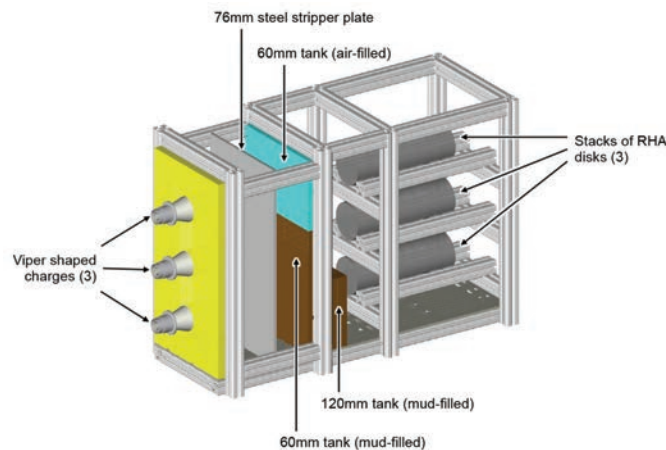


Fig. 1. Schematic representation of mud test setup.

**Stripper Plates.** It is important to conduct the jet erosion experiments in a velocity regime representative of the intended application. While the jet tip velocity for the LSCs under development can approach 6 km/s, the Viper jet tip velocity is around 9.2 km/s. To strip off the leading portions of the Viper jet so that the emerging tip will be closer to 6 km/s, 76mm of steel stripper plates were placed at one charge diameter (CD) standoff from the front face of the Viper charge. Though analytical equations for linearly stretching jets can be used to calculate jet tip erosion through materials of known density, the Viper jet tip does not behave linearly at early times; in particular, a 2 cm. region at the front of the jet does not follow a linear velocity profile [2]. Therefore, numerical simulations were used to determine the necessary thickness of these plates to achieve the reduced jet tip velocity.

**Mud Tank Design.** The mud tanks were designed to minimize the influence of any tank material and thereby isolating the effect of the mud on jet erosion. The tank walls were made of 3/16" polycarbonate. An empty tank was used in place of a mud-filled tank for the control jet to account for the nonzero jet erosion from the tank walls. Dimensional measurements of the tanks after filling were taken to verify the actual mud thickness for comparison to calculations. The drilling mud of interest is a heavy liquid with a nominal density of 16ppg ( $\sim 2 \text{ g/cm}^3$ ).

**Supporting Work.** Numerical simulations of Viper charges have previously been shown by LLNL to agree well with experimentation [2]. Images of the jet formation and measurements of the velocity profile compared well to calculations using the LLNL 2D hydrocode CALE. Current 2D simulations using LLNL ALE3D were found to match these results as well.

## MUD EROSION TEST AND SIMULATION SETUP

The dimensional layout of the experiment is shown in **Fig. 2**. All jets pass through identical thickness stripper plates to reduce the tip speed of the jets. Radiograph 1

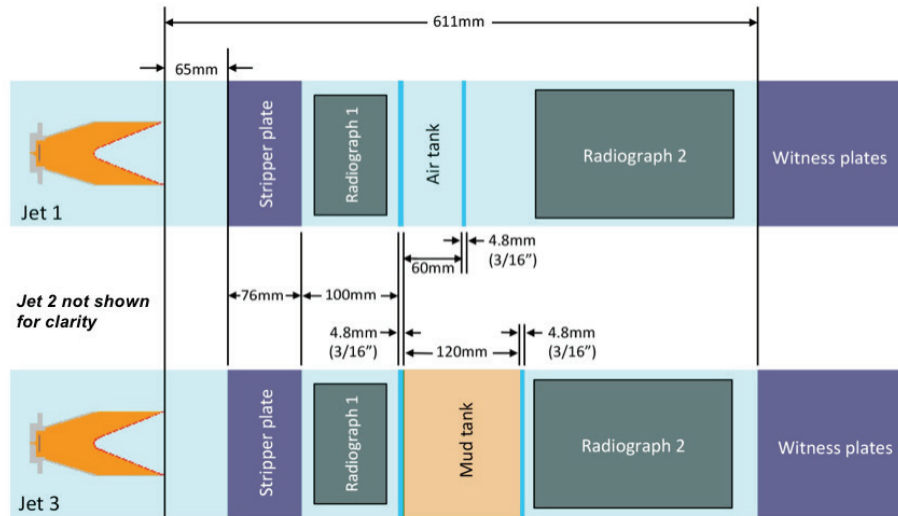


Fig. 2. Dimensional layout of experiment as used in simulations.

simultaneously visualizes all three jets and is taken at a time after the jets have emerged from the stripper plates and prior to entry into the tanks. Radiograph 2 is taken at a later time to capture the simultaneous tip locations of all three jets after emerging from their respective tanks. The upper Jet 1 is the control jet passing only through an air-filled tank, the middle Jet 2 passes through 60mm of mud, while the lower Jet 3 passes through 120mm of mud. A comparison of the differences in jet tip locations in Radiograph 1 indicates the simultaneity and reproducibility of the jets, while the differences in jet locations observed in Radiograph 2 indicate the erosion experienced by the jets traversing through 0, 60mm, and 120mm of drilling mud, respectively.

Initial computations of jets entering and exiting the varied mud tanks shown in **Fig. 2** were conducted to determine appropriate times to enable the radiographs to capture all three jets in the same image. The anticipated jet erosion in the mud is the primary unknown in these calculations.

The theory of shaped charge penetration [3] suggests that the single most important characteristic of the target material is its density. Therefore, in the absence of a well-understood material model for drilling mud, a model representing “heavy water” was used in which the density was scaled from 1.0 g/cm<sup>3</sup> to 2.0 g/cm<sup>3</sup> while keeping the bulk modulus the same. This is believed to be an acceptable surrogate for the present erosion rate calculations.

**Figs. 3, 4, and 5** show calculated x-t diagrams for the three jets in the mud test compared to an unimpeded Viper jet (constant tip velocity). The boundaries of the stripper plates, tanks, and witness plates are shown with dashed lines; changes in slope of the line representing the jet tip indicate the rate of erosion from whichever medium the jet is passing through.

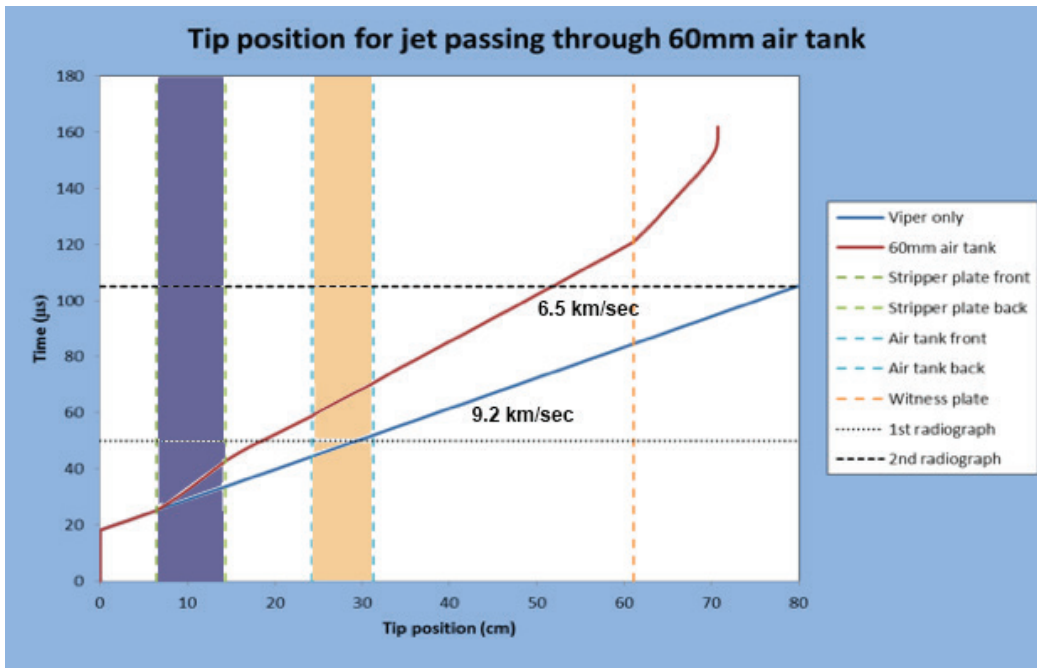


Fig. 3. Tip position for jet passing through 60mm air tank.

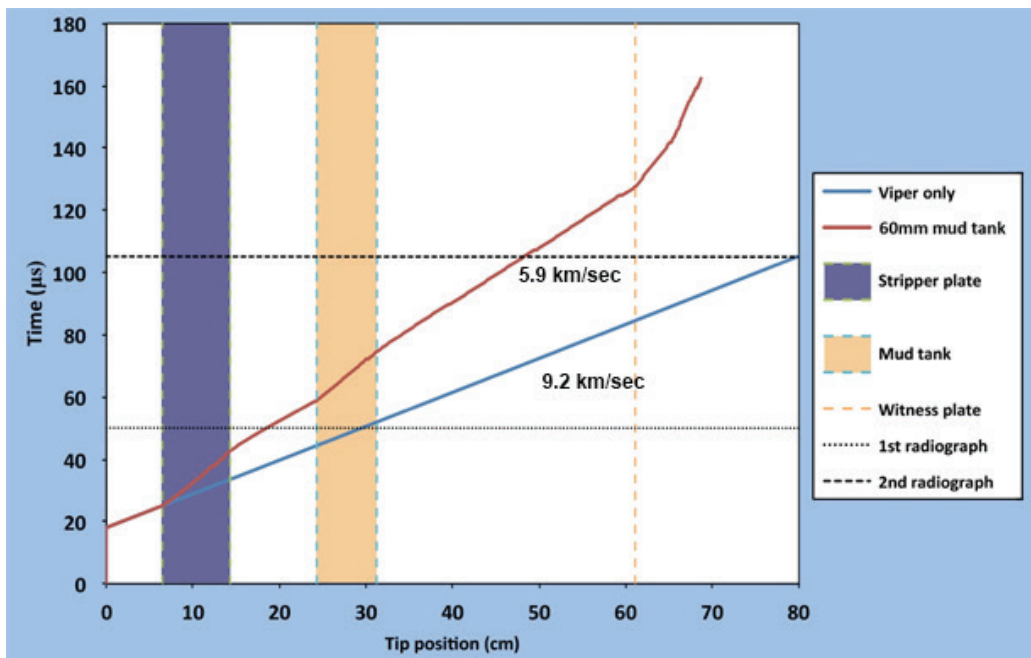


Fig. 4. Tip position for jet passing through 60mm mud tank

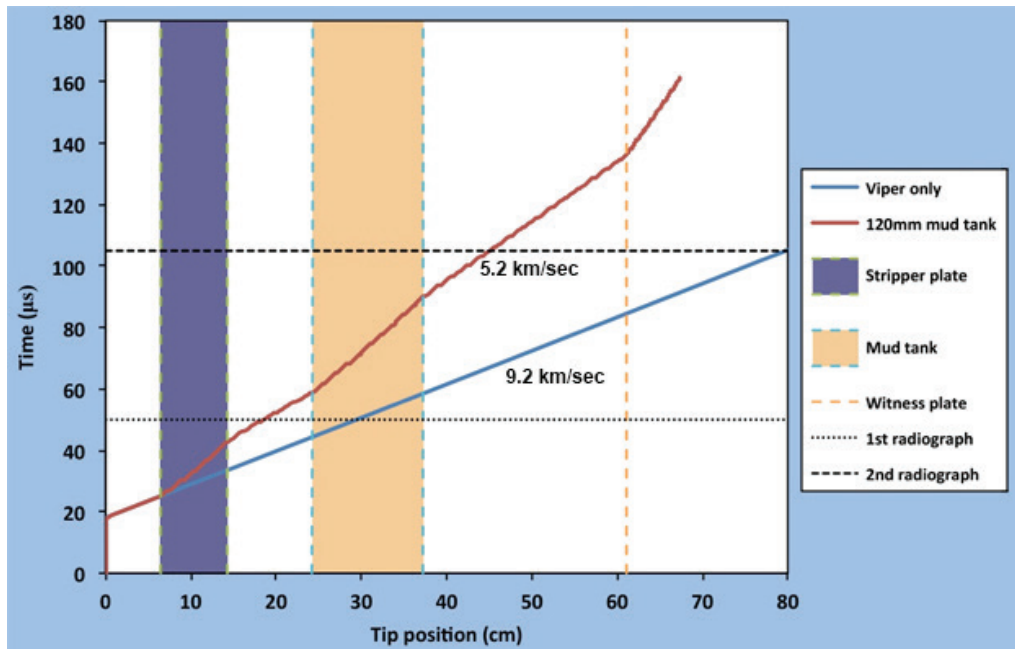


Fig 5. Tip position for jet passing through 120mm mud tank.

The red lines in the above figures are the calculated jet tip trajectory, while the blue line is the unimpeded Viper jet.

### EXPERIMENTAL RESULTS

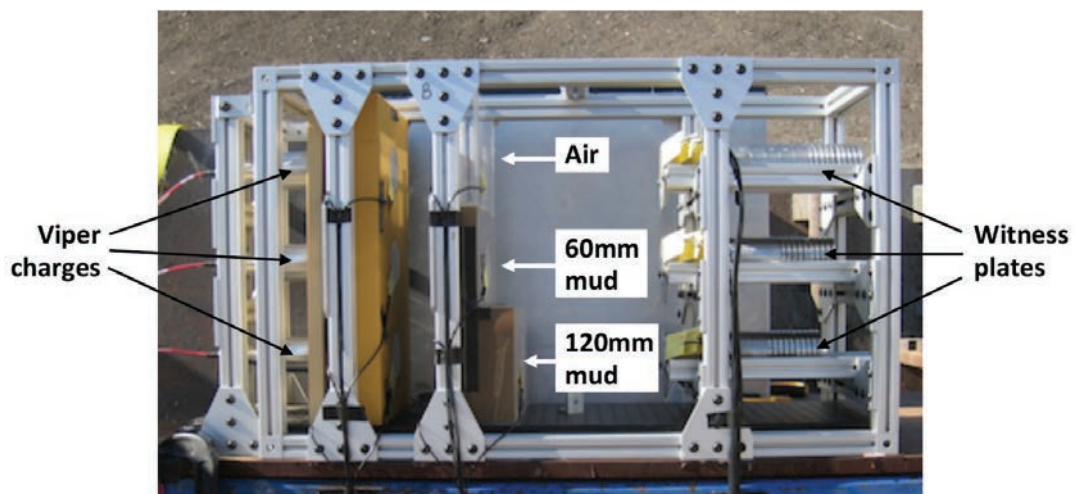


Fig. 6. Photo of Mud Test, ready to fire.

**Fig. 6** shows the relationship of the three Viper charges, stripper plates supported in rigid foam, the three tanks, and the stacked witness plates.

**Fig. 7** shows the radiographic images taken from Test B. The image shown is a mosaic of the two radiographs taken for each test; both images successfully captured the jet tips as intended. Fiducial markers which provide distance references in the path of the jets, consist of crossed and vertical 0.010" tungsten wires and can be seen in the image. The timing of the radiographs for Mud Test B was 56 $\mu$ s and 110 $\mu$ s to center the jets in the field of view of the radiographs.

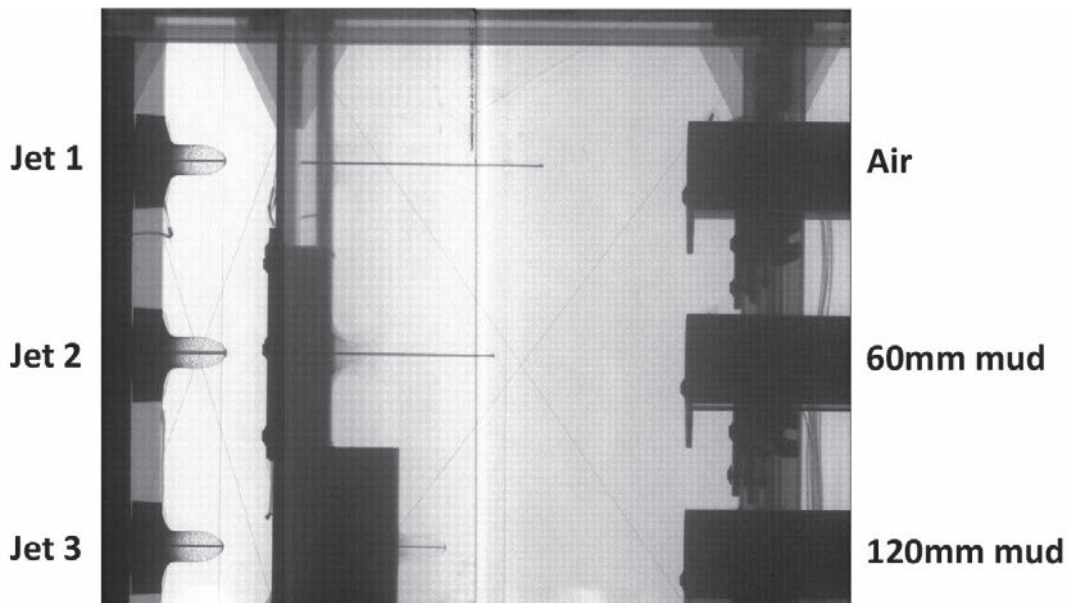


Fig. 7. Radiograph mosaic from Mud Test B.

The experimentally measured jet tip positions relative to the front face of the shaped charge are obtained from high-resolution analysis of the radiographs referencing the spatial fiducials in the image. The results of the jet tip position data analysis are shown in Table 1, along with the predicted values. The agreement between simulations and measured jet tip positions is quite good for all radiograph images, with differences of less than 2% for all jets after exiting both air and mud-filled tanks. Subtraction of jet tip positions after exiting the tanks provides a direct measure of length of jet eroded in the mud. Again, differences between simulation and data are small. In-situ measurement of the mud density was not made on these tests beyond a nominal 16 lb/gallon ( $\sim 2\text{g/cm}^3$ ) and noted as a requirement on future tests.

Time-of-arrival (TOA) screens successfully captured data of jet arrival at tank walls and target plates. These screens are sensitive to premature reporting due to debris outrunning the jets, and late reporting on the exit side as the screen is subject to expansion from material motion prior to being perforated by the jet. Data points taken from these TOA screens on two identical tests are overlaid on the predicted jet tip positions from simulations in **Fig. 8** and show good agreement with the overall simulation of jet trajectories. Note there is one delayed response on Test A, which is on the exit side of the 120mm mud tank, and not unexpected, as described above.

Table 1. Predicted and actual jet tip positions for Mud Test B (56 $\mu$ s and 110 $\mu$ s). Tip positions are measured from the front face of the charge in its initial configuration.

	Radio graph	Time ( $\mu$ s)	Sim.	Position (mm)		Sim.	Erosion (mm)	
				Actual	% Diff.		Actual	% Diff.
B1, 2, 3	Before mud	56	196.15	201.38	-2.59	–	–	–
B1	No mud	110	486.88	494.06	-1.45	–	–	–
B2	60mm mud	110	453.61	459.71	-1.33	33.3	34.4	-3.3
B3	120mm mud	110	417.51	425.73	-1.93	69.4	68.3	1.5

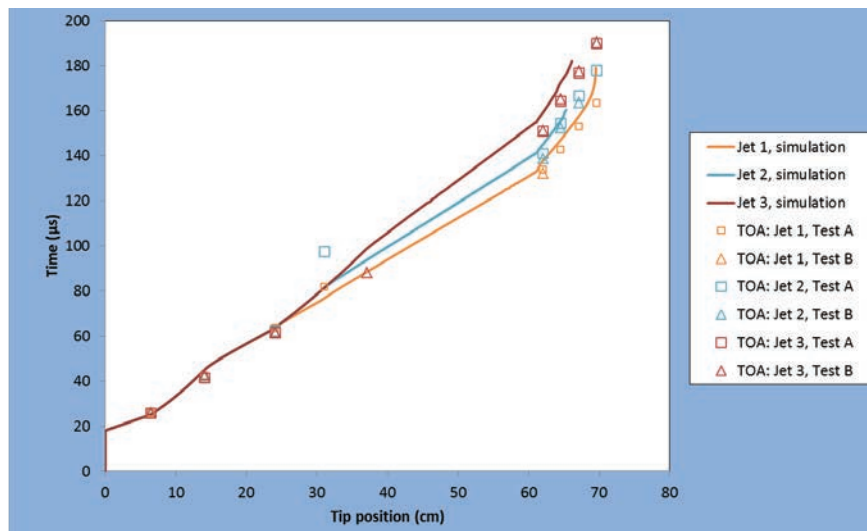


Fig. 8. Position-time diagrams for three jets with time-of-arrival (TOA) data.

**Jet Erosion in Mud Conclusions.** Two experiments to assess erosion rates of shaped charge jets in drilling mud were designed and conducted successfully with fully functioning diagnostics. Data obtained from these experiments were captured for comparison to simulations. Comparison of simulated and measured jet erosion showed that modeling drilling mud as water with a density of 2.0g/cm<sup>3</sup> is adequate for accurate simulation of shaped charge jet erosion in the velocity regime of interest to this problem. While these tests were conducted with unconfined and unpressurized mud, the conclusion that jet erosion can be accounted for based solely on mud density allows for simulations at downhole conditions using the appropriate downhole mud density.

### APPLICATION OF TECHNIQUE TO PERFORATOR CHARGE PERFORMANCE EVALUATION

A small variation of this test configuration is proposed to evaluate the dynamics of the interaction of perforator jets with varying thicknesses of concrete or geologic material. Comparison of simulated and measured jet erosion in selected portions of the jet can lead to improved perforator charge design

and efficiency. For simplicity of comparison, the same three-charge setup will be discussed, however, a different number of charges can be used with the same methodology.

The multi-charge array can be designed to characterize the penetration of individual sections of a perforator jet, when penetrating a target material of interest. The first design step is to determine the total depth of penetration ( $P$ ) into the target material of interest. Then the array (as shown in **Fig. 9** using 3 charges) would measure incremental jet erosion in the leading half of the jet from radiographs of the jet tip before and after penetrating material thicknesses of 0, 0.25 $P$ , and 0.5 $P$ . Additional target thicknesses of 0.7 $P$  and 0.9 $P$  could also be included in an array of 5 charges. Note that the maximum target thickness is selected as 0.9 $P$  rather than 1.0 $P$ , to allow the last portion of the jet to emerge from the target and be visible in the radiograph. These incremental thicknesses were chosen arbitrarily and can be selected as convenient. A single radiograph of the jets after exiting the incremental target materials provides a direct measure of jet erosion experienced by successive portions of the jet. The radiograph data can be tabulated as in Table 2 and used to assess an incremental penetration efficiency, which is defined as incremental penetration depth divided by observed jet erosion. Note a higher number represents more efficient penetration. An initial radiograph of all the jets prior to entering the targets can provide a reference point that all jets started simultaneously.

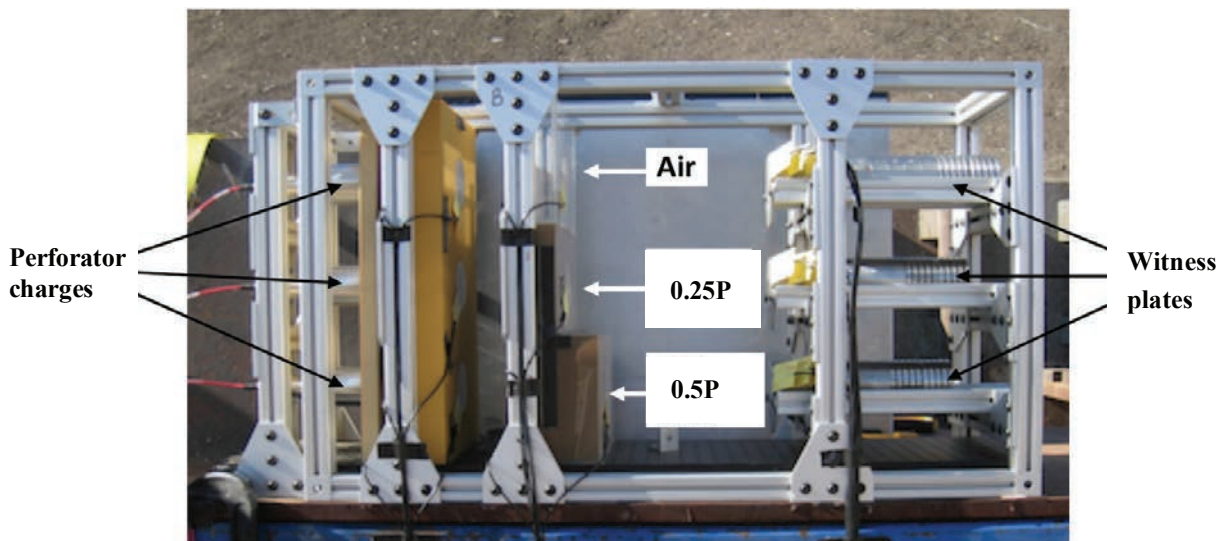


Fig. 9. Schematic of vertical test array configured for penetration efficiency tests of the leading portion of the perforator jet. Not to scale for geologic targets.

Table 2 shows a format for display of the data obtained for four different regions of the jet, using a reference of the jet tip position for Charge 1 propagating in free air. Using data from 5 charges (obtained from either one five-charge array or two 3-charge arrays), the penetration efficiency in the leading portion of the jet can be observed directly by comparing the erosion observed in jets 2 and 3. If penetration efficiency is constant between the first 25% and the second 25% of target thickness, the jet tip erosion (length of jet lost during 0.25 $P$  target penetration) in Table 2 will be identical for charges 2 and 3. Similarly for charges 4 and 5, which both penetrate 0.2 $P$  of target material, the relative penetration efficiency can be determined over the entire length of jet.

Table 2. Data table for determining incremental penetration efficiencies of different portions of perforator jets.

Charge	Target	X-ray time	Jet tip position (mm)	Jet tip erosion (mm)	Incremental Penetration efficiency
1	0	$t_1$	$z_1$	-	-
2	0.25P	$t_1$	$z_2$	$z_1-z_2$	$0.25P / z_1-z_2$
3	0.5P	$t_1$	$z_3$	$z_2-z_3$	$0.25P / z_2-z_3$
4	0.7P	$t_1$	$z_4$	$z_3-z_4$	$0.2P / z_3-z_4$
5	0.9P	$t_1$	$z_5$	$z_4-z_5$	$0.2P / z_4-z_5$

## CONCLUSION

While this test was initially designed to provide an effective method of determining penetration in heavy muds, there are clearly good synergies with the application of perforators in wells. There is well established value in being able to provide empirical validation of current physics models and penetration models.

## REFERENCES

1. Baum, D., G. Schebler, D. Dobie, D. Faux, R. Kuklo, 2016, "Characterization of Shaped Charge Jet Erosion in Drilling Mud," 29<sup>th</sup> International Symposium on Ballistics, May 9-13, 2016.
2. Baum, Dennis W., Larry L. Shaw, S. Christian Simonson, and Kris A. Winer. "Liner Collapse and Early Jet Formation in A Shaped Charge." 14<sup>th</sup> International Symposium on Ballistics, 1993.
3. Walters and Zukas (1998) "Fundamentals of Shaped Charges", Pg. 133, CM

LLNL-CONF-xxxxx

This work performed under the auspices of the U.S. Department of Energy by Lawrence Livermore National Laboratory under Contract DE-AC52-07NA27344.



# Analyzing API RP 19B, Section 4 Perforation Flow Testing Data – Part 1

Jacob A. McGregor, Halliburton-Jet Research Center

## BIOGRAPHICAL SKETCH

Jacob McGregor is a Sr. Petrophysical Applications Engineer, who has been working at Halliburton's Advanced Perforating Flow Laboratory for over 5 years. Before working at Halliburton, he worked as an on-site well fracturing engineer, performing hydraulic fracture stimulation treatments in the Marcellus Shale formation of Pennsylvania. He received a B.Sc. degree in petroleum engineering from The University of Texas at Austin in 2011 and is a Licensed Professional Engineer in the State of Texas.

## ABSTRACT

As part one of a two-part article discussing procedures for analyzing API RP 19B, Section 4 perforation flow testing data, the various Section 4 pre- and post-shot core characterization measurements are introduced and emphasis is placed on the pre-shot core permeability determination methodologies.

Convenient formulations of the quadratic Forchheimer equation are presented for linear, radial, and hemispherical flow geometries. These formulations account for various effects that may affect the equation's ability to model fluid flow through porous media such as the presence of multiple fluid phases and changing rock and fluid properties as a function of pressure.

We give two examples that apply the Forchheimer plotting method for the determination of the core's axial Darcy permeability while accounting for non-Darcy (inertial) effects: one flowing a gas, the other flowing a liquid. Methods that can be used to determine the core's diametral Darcy permeabilities are introduced, and examples are given on how to determine a core's principal permeabilities and axes of anisotropy in its transverse plane. The formulations presented herein are relevant to analyzing pre-shot and post-shot flow, the latter of which is developed further in the second part of the article.

## 1. INTRODUCTION

Since its inception, the fundamental law of flow through porous media given by Darcy (1856) has been scrutinized greatly and has been the subject for many modifications to take into account factors that are not considered in the original law (Civan, 2011). Darcy originally formulated the equation based on a specific set of conditions and assumptions, thus using the law explicitly as originally stated is limited in applicability. For API RP 19B Section 4 testing, many different flowing environments and boundary conditions are tested, requiring alternate and extended forms of Darcy's equation to analyze the flow data. These alternate formulas and the assumptions made to arrive at their derivation are multifarious.

.....

The current API RP 19B, Section 4 manual (API, 2014) states that "the choice of the data reduction analysis will depend upon the goals of the testing program and shall be left to the discretion of the testing company." While in agreement with this statement, it is beneficial to share and discuss how Section 4 flow data may be analyzed in ways not discussed in the current API RP 19B manual. Flow testing is conducted on the core both before and after it is perforated, the data from which is used to characterize its flowing properties. The data acquired from the pre-perforated testing can be used to: (1) characterize the core in terms of permeability and normalize the post-perforated flow testing data and (2) determine the magnitude of underbalance pressure required for perforation cleanup. The data acquired from the post-perforated testing can be used to: (1) provide a semi-quantitative indication of the net merit of a candidate perforating technique or (2) fully quantify the single-shot perforation skin.

Measurement of the directional permeability properties of the core is required to accurately analyze and quantify the single-shot perforation skin. Therefore, one of the primary aims of this article is to briefly highlight some of the key aspects of the tensorial nature of permeability, its directional nature, the various methods used to measure directional permeabilities and the determination from which the principal coefficients of the permeability tensor.

Another primary aim is to introduce convenient formulations of the quadratic Forchheimer equation for linear, radial, and hemispherical flow geometries. The linear flow geometry is relevant for both pre-shot and post-shot flow performance evaluations. The radial and hemispherical flow geometries are relevant for post-shot flow performance, the relevance of which will be developed further in the second part of the article. In this way, the foundational equations for post-shot flow evaluations to be discussed in the second article are introduced here.

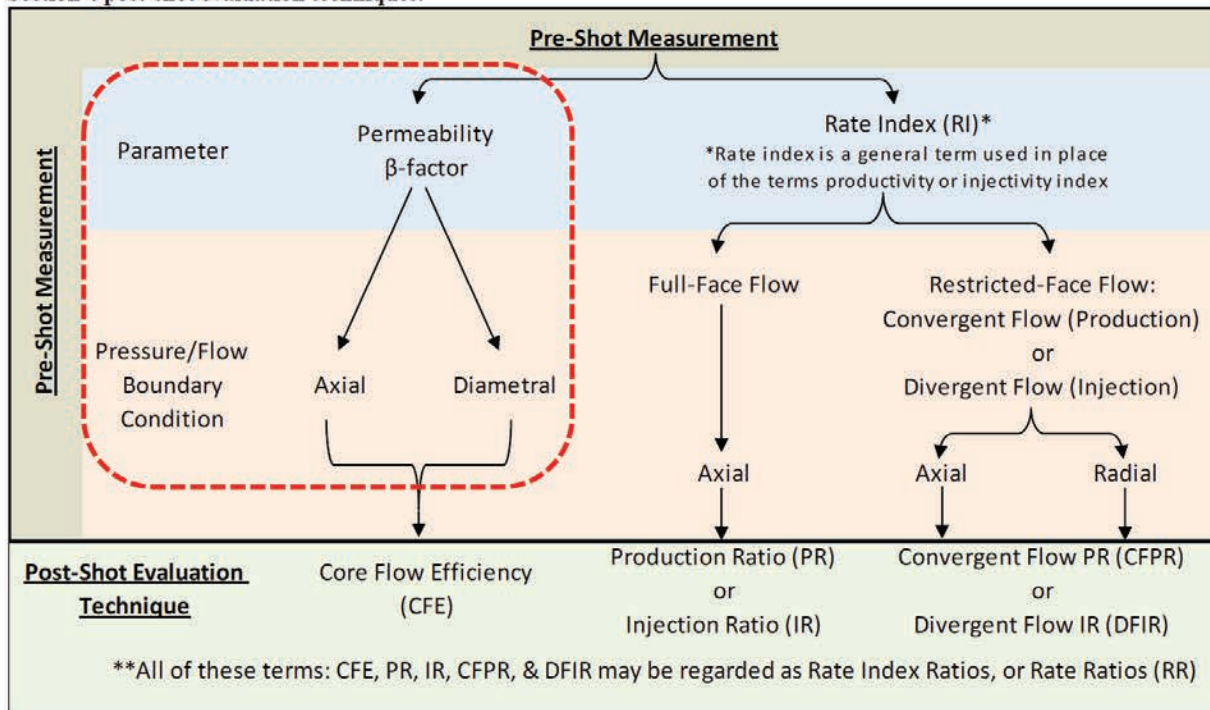
Furthermore, much of the historical pre-shot directional permeability determination procedures are based on Darcy's law. Thus, the pressure-flow relationship for the rock is characterized with a single (multi-component) parameter, the permeability tensor, which models flow accurately when the flow is dominated by viscous forces. However, during the perforation event large pressure differentials drive high flow rates which generate large inertial forces. The ability of Darcy's law to model such flow decreases, and Forchheimer's equation, which includes an additional rock characterization parameter, the  $\beta$ -factor, more appropriately models the pressure-flow relationship. Since flow into a perforation is three-dimensional, there may be significant understandings to be gained by assessing the directional nature of the  $\beta$ -factor, especially for the determination of the critical underbalance pressure required for perforation cleanup using a physics based model such as Tariq's (1990).

Therefore, the objectives of this article are to (1) partially expand and elaborate on the methods given in the current API RP 19B, Section 4 manual for characterizing the rock target in terms of permeability and  $\beta$ -factor, and (2) set the foundation on which a subsequent article is to be given on the analysis of post-perforated flow data.

## 2. CHARACTERIZING THE ROCK TARGET FOR SECTION 4 TESTING

As the Section 4 manual states, the pre-shot flow measurements required for a particular test program strongly depends on the type of final flow performance evaluation technique to be used. Figure 1 is a flow chart illustrating the various pre-shot core characterization measurements, the boundary conditions that are imposed, and the corresponding post-shot evaluation techniques. As seen highlighted in the red box, to perform the post-shot CFE evaluation technique multiple pre-shot permeability measurements are required to characterize the core's permeability anisotropy, which is then used to calculate the core's post-shot theoretical (i.e. "perfectly clean") rate index, which is determined either analytically or by numerical modeling (Grove et al. (2012)).

Figure 1. Illustration of the various pre-shot core characterization methods and how they can be used for the various Section 4 post-shot evaluation techniques.



Accordingly, the characterization of a rock target's permeability anisotropy prior to perforating while taking into account non-Darcy (inertial) forces is one of the primary subjects of this paper.

## 3. ANISOTROPIC PERMEABILITY

The permeability of a sedimentary rock is anisotropic as a result of various depositional and sometimes post-depositional processes. For example, at the microscopic scale the deposition of irregularly shaped rock particles produce preferred orientations of grain and pore long axes within a bedding plane, producing a directional permeability anisotropy within the bedding plane. At the macroscopic scale, a rock composed of thin layers of various permeabilities yields anisotropic permeability. Larger scale anisotropy may result from heterogeneities at smaller scales. In this way, anisotropy, like heterogeneity,

is a scale-dependent property of naturally-occurring porous media (Lake, 1988). When certain criteria are met (e.g., see Long et al. (1982)), rocks that are heterogeneous at a scale smaller than the rock volume being evaluated are modeled as macroscopically homogeneous anisotropic rocks for mathematical convenience (Morita N. , 1974; Bear, 1988). The anisotropic permeability formed is usually considered to be a symmetric 2<sup>nd</sup>-rank positive-definite tensor. The general absolute Darcy permeability tensor  $\bar{\bar{k}}_d$  is represented by a 3 x 3 matrix of scalars, which in an arbitrarily selected 3D Cartesian coordinate system is

$$\bar{\bar{k}}_d = \begin{bmatrix} k_{d,xx} & k_{d,xy} & k_{d,xz} \\ k_{d,yx} & k_{d,yy} & k_{d,yz} \\ k_{d,zx} & k_{d,zy} & k_{d,zz} \end{bmatrix} \quad (1)$$

The tensor is symmetric and as such  $k_{d,ij} = k_{d,ji}$  ( $i, j = x, y, z$  or  $1, 2, 3$ , or  $x_1, x_2, x_3$ ). The diagonal coefficients are casually referred to as the normal permeability coefficients, and the off-diagonal coefficients as the cross permeability coefficients (Haque, 2015). An important property of a symmetric tensor is that by a suitable rotation of axes, it is possible to transform the full tensor into another tensor consisting of only diagonal terms. The axes that permit this transformation are called the principal axes (the eigenvectors of the tensor). These principal axes contain the maximum, intermediate, and minimum values of the directional permeabilities. These are the diagonal terms of the transformed tensor (the eigenvalues of the tensor). Thus, when the  $x, y, z$  axes of the 3D Cartesian coordinate system are co-linear with the principal directions of permeability anisotropy the permeability tensor becomes (Peters, 2012)

$$\bar{\bar{k}}'_d = \begin{bmatrix} k'_{d,x} & 0 & 0 \\ 0 & k'_{d,y} & 0 \\ 0 & 0 & k'_{d,z} \end{bmatrix} \quad (2)$$

Typically, the minimum principal permeability coefficient is approximately perpendicular to the bedding plane, and the other two principal permeability coefficients are approximately parallel to the bedding plane. The true direction of the principal axes cannot be known *a priori*, thus directional permeability assessments must be made.

#### 4. DIRECTIONAL PERMEABILITY

The superficial velocity vector  $\vec{v}$  is only parallel to the fluid potential gradient vector  $\vec{J}$  ( $\equiv -\nabla\Phi$ ) along the principal axes of the tensor due to the fact that permeability is a 2<sup>nd</sup>-rank tensor. For an unbounded anisotropic medium (Figure 2A), where a hypothetical steady flow condition is considered, Scheidegger (1957) showed that there are two limiting expressions for how the directional permeability may be defined. Using Figure 2B as reference, if the permeability is expressed as the ratio of the magnitude of the superficial velocity vector to the component of the potential gradient vector in the direction of the flow,

$$k_v = \mu|\vec{v}|/(|\vec{J}|\cos\theta), \quad (3)$$

then the directional permeability in the direction of flow is given by the relation (Bear, 1988)

$$\frac{1}{k_v} = \frac{\cos^2 \beta_x}{k'_{d,x}} + \frac{\cos^2 \beta_y}{k'_{d,y}} + \frac{\cos^2 \beta_z}{k'_{d,z}} \quad (4)$$

where  $k_v$  is the (scalar) directional permeability in the direction of flow,  $k'_{d,x}$ ,  $k'_{d,y}$ , and  $k'_{d,z}$  are the three principal coefficients of the permeability tensor, and  $\beta_x$ ,  $\beta_y$  and  $\beta_z$  are the angles between the direction of flow and the three principal axes,  $x$ ,  $y$ , and  $z$ , respectively. The direction cosines in Eqn (4) produce an ellipsoidal representation quadric (Nye, 1957) of the diagonalized tensor, where  $\sqrt{k_v}$  is represented graphically as a function of the directions of  $\vec{v}$  to produce an ellipsoid.

If the permeability is expressed as the ratio of the component of the superficial velocity vector in the direction of the potential gradient vector to the potential gradient,

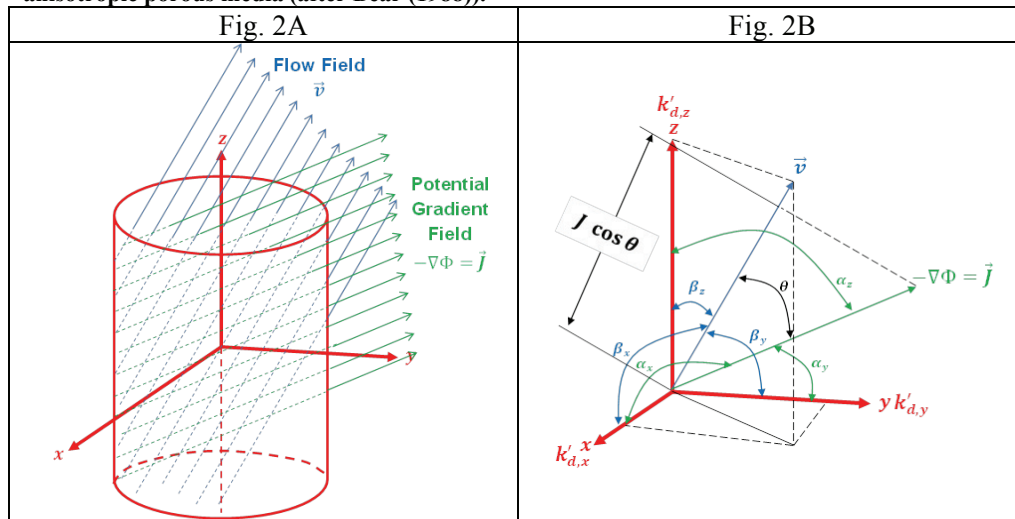
$$k_J = \mu |\vec{v}| \cos \theta / |\vec{J}|, \quad (5)$$

the (scalar) directional permeability in the direction of the gradient,  $k_J$ , is given by the relation (Bear, 1988)

$$k_J = k'_{d,x} \cos^2 \alpha_x + k'_{d,y} \cos^2 \alpha_y + k'_{d,z} \cos^2 \alpha_z \quad (6)$$

where  $\alpha_x$ ,  $\alpha_y$  and  $\alpha_z$  are the angles between the direction of the potential gradient and the three principal axes,  $x$ ,  $y$ , and  $z$ , respectively. The direction cosines in Eqn (6) produce an ellipsoidal representation quadric of the diagonalized tensor, where  $1/\sqrt{k_J}$  is represented graphically as a function of the directions of  $\vec{J}$  to produce an ellipsoid. Thus, there are two definitions of directional permeability; values from which are not the same unless measurements are made with  $\vec{v}$  and  $\vec{J}$  in the direction of one of the principal axes.

Figure 2. (A) An unbounded anisotropic medium, under hypothetical steady flow. (B) General flow conditions in anisotropic porous media (after Bear (1988)).



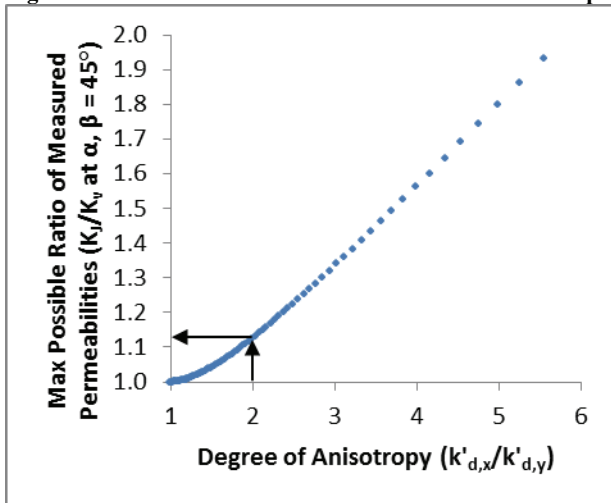
Assuming the bedding planes to lie in the x-y plane, and assuming the direction perpendicular to the bedding planes to be one of the principal permeability directions, then for 2D anisotropic flow within the x-y plane Eqns (4) and (6) can be written as Equation (7) and (8), respectively.

$$\frac{1}{k_v} = \frac{\cos^2 \beta_x}{k'_{d,x}} + \frac{\cos^2 \beta_y}{k'_{d,y}} \tag{7}$$

$$k_J = k'_{d,x} \cos^2 \alpha_x + k'_{d,y} \cos^2 \alpha_y \tag{8}$$

Plots of  $\sqrt{k_v}$  or  $1/\sqrt{k_J}$  versus angle on polar graphs will be ellipses according to Eqns (7) & (8), respectively. Scheidegger (1957) analyzed the ratio,  $k_J/k_v$ , of these two limiting 2D permeability expressions for their maximum deviation (which occurs when  $\beta_x$  or  $\alpha_x = 45^\circ$ ). From his analysis he showed that the ratio of the principal permeabilities,  $k'_{d,x}/k'_{d,y}$  ( $k'_{d,x} > k'_{d,y}$ ) must be appreciable before the error committed by interchanging the two types of directional permeabilities becomes significant, e.g., when  $k'_{d,x}/k'_{d,y} = 2$ ,  $k_J/k_v = 1.125$  (Figure 3). He concluded that in most cases it is not necessary to distinguish between  $k_v$  and  $k_J$ .

**Figure 3. Maximum variation of measured directional permeabilities as a function of anisotropy (after Parsons (1964)).**



Combining the explanations of (Bear, 1988; Caldwell, 1971; Snow, 1965; Parsons, 1964), the physical representations of these two limiting expressions for directional permeability are given as follows: Cut from the anisotropic medium a (hypothetical) long and narrow cylinder ( $L/D \rightarrow \infty$ ), apply a no-flow boundary on its cylindrical surface (Figure 4A, next section), and measure its permeability in the usual way. In this case the flow velocity vector must be compelled along the cylinder's axis. However, with such boundaries the potential gradient is unknown, the equipotentials are generally oblique to the core's axis. This situation is a representation of the sort of test that would yield a value for  $k_v$ , and therefore Eqn (4) (or Eqn (7)) is applicable. Cut a pancake-like cylinder ( $D/L \rightarrow \infty$ ) from the medium, apply a no-flow boundary on its cylindrical surface (Figure 4A, next section), and measure its permeability in the usual

way. In this hypothetical case the effects of the no-flow boundary are negligible, the potential gradient is practically parallel to the normal to the broad planar-faces of the cylinder. The gradient vector is known, while the velocity vector is generally oblique to the equipotentials and inclined to the principal axes of permeability (the fluid will move in the direction of least resistance). This situation is a representation of the sort of test that would yield a value for  $k_J$ , and therefore Eqn (6) (or Eqn (8)) is applicable.

For cylinders having intermediate length-to-diameter ratios, the measured directional permeability does not equal either of the two limiting scenarios as defined above. The issue concerning which directional permeability is measured in the laboratory where a no-flow boundary condition is imposed on an anisotropic sample of finite length and width (diameter) has been explored in depth by Marcus and Evenson (1961), Marcus (1962), and Morita (1974). When a no-flow boundary condition is applied (i.e. when using a permeameter) the directional permeability measured is neither in the direction of flow nor in the direction of the potential gradient (unless the direction of flow is collinear with one of the principal axes). Therefore, the directional permeability actually measured is referred to as an apparent directional permeability (Marcus, 1962; Parsons, 1964).

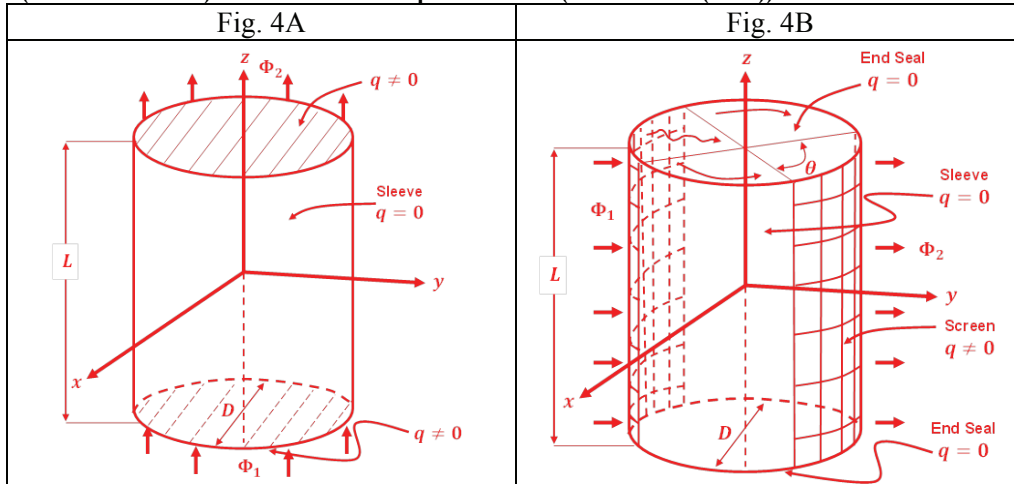
Studying 2D anisotropic flow through a sample of finite dimensions with boundary conditions similar to Figure 4A, next section), Marcus and Evenson (1961) and Marcus (1962) show that  $k_J \geq k_v$ . They presented graphs plotting the percentage difference between  $k_J$  and  $k_v$  as a function of the degree of anisotropy,  $k'_{d,y}/k'_{d,x}$  ( $k'_{d,x} > k'_{d,y}$ ). The difference between the two directional permeabilities, as defined by the flow and gradient directions, is 10% when  $k'_{d,y}/k'_{d,x} = 0.5$  and when the flow or gradient vector is inclined  $45^\circ$  from a principal axis. The percentage difference between the two directional permeability definitions increases rapidly for greater degrees of anisotropy, that is, as  $k'_{d,y}/k'_{d,x} \rightarrow 0$ .

In light of the foregoing review, when measuring permeability using a permeameter having boundary conditions similar to Figure 4A (next section), a core that has a geometry ratio  $L/(\sqrt{\pi}r) > 1$  is considered "long," and the permeability realized is closer to the definition given for the directional permeability in the direction of flow  $k_v$  (Morita N. , 1974; Morita & Gray, 1980). Likewise, a core having a geometry ratio  $L/(\sqrt{\pi}r) < 1$  is considered "short," and the permeability realized is closer to the definition given for the directional permeability in the direction of the gradient  $k_J$ .

## 5. PERMEAMETERS AND BOUNDARY CONDITIONS

The two types of permeameters discussed here are those that have boundary conditions as those shown in Figure 4, which are referred to here as the axial permeameter (Figure 4A) and the diametral (radial transverse) permeameter (Figure 4B).

Figure 4. (A) Boundary conditions for axial flow in an axial permeameter, (B) Boundary conditions for diametral (radial transverse) flow in a diametral permeameter (after Morita (1974)).



When using the axial permeameter, constant fluid potentials,  $\Phi_1$  and  $\Phi_2$ , are applied across the planar-ends of the core, and a no-flow boundary condition is applied on the core's cylindrical surface. When using the diametral permeameter, constant fluid potentials,  $\Phi_1$  and  $\Phi_2$ , are applied across opposing segments of the core's cylindrical surface (denoted as "screen" in Figure 4B, and span the entire length of the core), which permit fluid flow across said surface. The width of the screen subtends an angle  $\theta$ . All other portions of the core's surface are sealed so that there is no flow across the remaining boundaries.

The axial and diametral permeabilities of the whole core perforated in a Section 4 test can be evaluated using the axial permeameter alone, or by using both the axial and diametral permeameters. For the former, referred to as "Method 1," the axial permeability of the whole core is determined. Smaller cores (plugs) are cut transverse to the axis of the whole core and the axial permeabilities of these plugs are measured, which produce the directional permeabilities transverse to the whole core's long axis. For the latter, "Method 2," the axial permeability of the whole core is determined and the diametral permeameter is used to measure the directional permeabilities transverse to the whole core's long axis.

With the permeability tensor, directional permeability, and the two types of permeameters considered now defined, the aim of the following sections, in order, is to: (1) introduce a generalized quadratic Forchheimer equation, (2) develop convenient formulations of the Forchheimer equation for determining the directional permeability while using the axial permeameter, (3) describe the graphical approach for determining the (directional) Darcy permeability and (directional) Forchheimer  $\beta$ -factor while using the axial permeameter, (4) provide examples of application of the aforementioned graphical approach, (5) describe an analysis procedure for determining the maximum and minimum diametral directional permeability values when performing Method 1 for the determination of the permeability tensor principal coefficients, and (6) provide comment on the use of the diametral permeameter to measure the directional permeabilities transverse to the whole core's long axis (Method 2).

## 6. FLUID MOTION EQUATION

Following the formulations given by Bear and Cheng (2010), Evans and Evans (1988), and Cooper et al. (1999), the differential macroscopic fluid momentum balance ( $\equiv$  flow) equation, used to describe three-dimensional flow of multiple immiscible, Newtonian, compressible and incompressible fluids through a homogeneous, anisotropic, porous medium, may be written as

$$-\nabla\Phi_\alpha = \mu_\alpha(\bar{\mathbf{k}}_d k_{r\alpha})^{-1} \cdot \vec{\mathbf{v}}_\alpha + \rho_\alpha \bar{\boldsymbol{\beta}}_\alpha \cdot \vec{\mathbf{v}}_\alpha |\vec{\mathbf{v}}_\alpha| \quad (9)$$

$\vec{\mathbf{v}}_\alpha$  is the superficial velocity vector of fluid phase  $\alpha$ , with  $\alpha$  being the fluid phase index;  $\bar{\mathbf{k}}_d$  is the absolute Darcy permeability tensor;  $k_{r\alpha}$  is the relative permeability to fluid phase  $\alpha$ ;  $\mu_\alpha$ ,  $\Phi_\alpha$ , and  $\rho_\alpha$  are the viscosity, fluid potential, and density of fluid phase  $\alpha$ , respectively, and  $\bar{\boldsymbol{\beta}}_\alpha$  is the coefficient of inertial resistivity tensor ( $\beta$ -factor tensor) to fluid phase  $\alpha$ .  $|\vec{\mathbf{v}}_\alpha|$  is the  $l^2$ -norm (magnitude) of the superficial velocity vector, which allows  $\beta$  to be written as a tensor quantity. The product  $\bar{\boldsymbol{\beta}}_\alpha |\vec{\mathbf{v}}_\alpha|$  makes Equation (9) quadratic with respect to superficial velocity.

Equation (9) is the commonly cited quadratic Forchheimer equation\* (see Dupuit (1863) and Forchheimer (1901)) extended to account for three-dimensional multiphase flow. The Forchheimer equation, like Darcy's equation, originated empirically from experiments. Nevertheless, when assuming single phase flow both equations have been analytically derived in several ways, primarily on the foundations of dimensional analysis, control volume balance, and from the Navier-Stokes equations using volume averaging and homogenization principles. Each accounts for a set of assumptions about the nature of the flow (Bear, 1988; Civan, 2011). Since Eqn (9) describes the simultaneous flow of immiscible fluids, it is a working assumption, postulated using channel flow theory (Willhite, 1986) or heuristics. Regardless, it models multiphase flow with sufficient accuracy for all practical purposes.

For single-phase flow and assuming a Cartesian  $(x, y, z)$  coordinate system, Eqn (9) can be reduced to the commonly cited quadratic Forchheimer equation for one-dimensional flow (Eqn (10)) under the following assumptions and conditions:

1. The coordinate system is chosen such that the  $x, y, z$  coordinates coincide with the principal axes of permeability anisotropy.
2. The principal axes of inertial resistivity anisotropy coincide with the principal axes of permeability anisotropy.
3. The fluid potential gradient vector  $\nabla\Phi$  is collinear with the  $z$  axis; and
4. The flow rate is designated as positive and moves in the positive  $z$ -direction.

---

\* From empirical observations Forchheimer (1901) noted that the pressure gradient can be related to a second order polynomial in velocity,  $\alpha = av + bv^2$ , where he denoted  $a$  and  $b$  as constants, and  $\alpha$  as the pressure gradient. Green & Duwez (1951) separated the coefficients of the linear and the square terms of Forchheimer's equation into fluid and porous matrix parameters by dimensional analysis, obtaining:  $-dp/dx = \alpha\mu v + \beta\rho v^2$ , where  $\alpha = 1/k_d$ .

$$-\partial\Phi/\partial z = \mu k'_{d,z}{}^{-1} v_z + \beta'_z \rho v_z^2 \tag{10}$$

Assuming the medium to be isotropic in  $k_d$  and  $\beta$ , the above equation can be simplified as,

$$-d\Phi/ds = \mu k_d^{-1} v + \beta \rho v^2 \tag{11}$$

where  $s$  is the distance in the direction of flow and is always taken as a positive value. The  $k_d$  term used here can be thought of as a generalized (or undefined) directional permeability, poised to be defined as equivalent to  $k_v$  or  $k_j$  once the flow conditions are defined. Treating Eqn (9) in terms of single-phase flow, assuming a Cartesian  $(x, y, z)$  coordinate system, and taking the inertial effects of the flow as negligible, Eqn (9) reduces to the commonly cited generalized Darcy equation for three-dimensional flow,

$$\vec{v} = -\mu^{-1} \vec{k}_d \cdot \nabla\Phi \tag{12}$$

Forchheimer's equation (Eqn. (11)) states that the total potential gradient driving flow is the sum of the viscous potential gradient ( $\mu v/k_d$ ) and the inertial potential gradient ( $\beta \rho v^2$ ). At "low" Forchheimer numbers,  $F_o = k_d \beta \rho v / \mu \leq 0.005$  (API, 1998) or  $F_o \leq 0.11$  (Zeng & Grigg, 2006), where inertial forces are considered small compared to the viscous forces, the Forchheimer equation reduces to Darcy's law (Eqn (12)), thus Darcy's law can be considered as a special case of the Forchheimer equation. This emphasizes the fact that inertial forces are always present whenever flow takes place through porous media, but they can be insignificantly small such that Darcy's law may be considered valid.

For the purposes of this paper, we neglect the gravitational and kinetic energies of Hubbert's (1940) fluid potential (normalized to volume),

$$\Phi = g \underbrace{\int_{z_o}^z \rho(z) dz}_{\text{gravitational energy}} + \underbrace{\frac{\rho v^2}{2}}_{\text{kinetic energy}} + \underbrace{\int_{p_o}^p dp}_{\text{pressure energy}} \tag{13}$$

and thus take pressure gradients as being very close approximations to fluid potential gradients for any flow orientation used while testing

$$\nabla p \cong \nabla\Phi \tag{14}$$

## 7. CONVENIENT FORMULATIONS OF THE FORCHHEIMER EQUATION FOR THE AXIAL PERMEAMETER

Equation (11) is written in differential form and, barring numerical solution, must be integrated to find a suitable equation to use for evaluating the flow data generated in Section 4 testing. In the process of integrating Eqn. (11) with respect to spatial position and pore pressure, we note that absolute permeability is a function of pore pressure through either the Knudsen-Klinkenberg (slippage) effect (Klinkenberg, 1941) and/or effective stress, and is altered by the presence of more than one fluid occupying the pore space. Additionally, fluid viscosity and density are pressure (and temperature) dependent. To handle these physical parameters during the integration of Eqn. (11), which are dependent on pressure, we use the Kirchhoff (1894) transformation (Carslaw & Jaeger, 1959; Ames & Ames, 1965). In petroleum engineering this integral transformation is referred to as pseudo-pressure (Russell et al. (1966), Al-Hussainy et al. (1966)). To account for these pressure-dependent variables, a normalized pseudo-pressure, following the definitions given by Russell et al. (1966) and Walsh & Lake (2003), can be defined as

$$m_{\alpha}(p) = \frac{\mu_{\alpha,n} B_{\alpha,n}}{k_{d,n} k_{r\alpha,n}} \int_{p_b}^p \frac{k_d k_{r\alpha}}{\mu_{\alpha} B_{\alpha}} dp + p_b \quad (15)$$

where the subscript  $n$  indicates the normalizing condition, where a normalizing pressure and temperature are arbitrarily selected to evaluate the normalizing variables (the variables denoted with the subscript  $n$ ) which make up the normalizing factor (the term before the integral). This normalizing factor is used to conveniently scale the pseudo-pressure transform, allowing the units of pressure to be retained (Walsh & Lake, 2003). The definite integral is computed using numerical integration (quadrature), e.g., using trapezoidal or Simpson's rule. A few comments are to be made with regards to use of this pseudo-pressure. (1) In general, since  $k_{r\alpha}$  is a function of saturation, and the saturation of phase  $\alpha$  is a function of pressure, it requires specification of the saturation-pressure path (i.e. saturation history). This makes the function difficult to evaluate analytically. Moreover, the spatial saturation distribution throughout the porous medium must be known. To alleviate the nuances of evaluating Eqn. (15),  $k_{r\alpha}$  is assumed as a fixed value and a property of the porous medium everywhere in space. This assumption is akin to flow taking place where pore pressure is above the fluids' bubble- and/or dew-point pressure(s), and no mass exchange takes place between fluid phases. For multi-fluid Section 4 testing it is common to condition cores with a fluid phase at a constant residual, non-flowing, saturation condition. This saturation state is achieved by displacing the designated non-flowing phase with the flowing phase using a pressure drop between 10% to 25% greater than the pressure drop to be used during pre-shot and post-shot flow testing (API, 2014). By doing so  $k_{r\alpha}$  is made to be a fixed value. (2) In general, permeability is a function of position (i.e. natural porous media is heterogeneous), but the idealized case of homogeneity is considered here. (3) Like saturation, the stress history of the porous medium and its effect on permeability makes the pseudo-pressure function difficult to evaluate analytically. To evaluate Eqn. (15) analytically, the porous medium can be assumed perfectly ridged or perfectly elastic. (4) Finally, when the pseudo-pressure function does not depend on the saturation-pressure path nor stress path, and the fluids are Newtonian and their viscosities are independent of their shear rate histories, pseudo-pressure is a state function which

depends on the current conditions of pressure and temperature at the spatial location within the medium. Due to the viscous nature of fluids and the Joule-Thomson effect, flow is rarely strictly isothermal (see the inlet and outlet temperatures in Figs 7B & 9B given in Section 9). Thus the pseudo-pressure function, the variables within the integral, should be evaluated at the fluid's spatial pressure and temperature condition.

The isotropic Forchheimer equation expressed in terms of pseudo-pressure and integrated using the linear flow geometry for positive direction flow is written as (0)

$$\Delta m_\alpha(p) = \frac{\mu_{\alpha,n} B_{\alpha,n} \bar{k}_{e\alpha}(\bar{p})}{k_{e\alpha,n}} \cdot \frac{q_{\alpha,sc} L}{\pi r^2} \left[ \frac{1}{k_{e\alpha}} + \frac{\beta_\alpha \rho_{\alpha,sc} q_{\alpha,sc}}{\pi r^2 \bar{\mu}_\alpha} \right] \quad (16)$$

Equation (16) is general with regards to accounting for stress and/or Klinkenberg apparent permeability effects and compressible multiphase flow. However, for Section 4 gas flow testing, it is common to test cores that have permeabilities greater than 0.1-1.0 md and to test with outlet flowing pressures greater than 300 psi. Thus, the Klinkenberg effect is generally negligible (You, Xue, Kang, Liao, & Kong, 2013; Hubbert, 1956). Likewise, it is common to test cores that are sufficiently stiff as to have negligible stress dependent permeability and  $\beta$ -factor qualities. Though, when testing weak (low unconfined compressive strength) cores, it is common to pre-stress the cores to an effective stress 10% to 25% greater than that which they would experience during the flow testing experiment. The purpose of this pre-stressing is to remove any inelastic deformation, and stress dependent permeability and  $\beta$ -factor attributes, prior to beginning the experiments. Therefore, if stress and/or Klinkenberg apparent permeability effects are negligible, Eqn (16) can be simplified to

$$\Delta m_\alpha(p) = \mu_{\alpha,n} B_{\alpha,n} \cdot \frac{q_{\alpha,sc} L}{\pi r^2} \left[ \frac{1}{k_{e\alpha}} + \frac{\beta_\alpha \rho_{\alpha,sc} q_{\alpha,sc}}{\pi r^2 \bar{\mu}_\alpha} \right] \quad (17)$$

where the pseudo-pressure has now been defined as:

$$m_\alpha(p) = \mu_{\alpha,n} B_{\alpha,n} \int_{p_b}^p \frac{1}{\mu_\alpha B_\alpha} dp + p_b \quad (18)$$

since permeability is no longer considered to be pressure dependent (the relative permeability is considered a fixed value and not pressure dependent). When only a single fluid phase occupies the pore space Eqn (17) (and Eqn (18)) can be simplified further by simply dropping the phase designation subscript  $\alpha$ . For tests flowing degassed liquids under approximately isothermal conditions and at relatively low differential pressures,  $\rho$  and  $\mu$  are approximately constant and therefore the pseudo-pressure analysis is not absolutely required. Consequently,  $\Delta m(p) \approx \Delta p$ , and other variables are taken as constants:  $q_{sc} = q$ ,  $\rho_{sc} = \rho$ ,  $B = 1$ , and  $\bar{\mu} = \mu$ . Therefore, Eqn (17) can be simplified even further,

$$\Delta p = \frac{qL}{\pi r^2} \left[ \frac{\mu}{k_d} + \frac{\beta \rho q}{\pi r^2} \right] \quad (19)$$

## 8. GRAPHICAL DETERMINATION OF THE PARAMETERS $k_d$ AND $\beta$ WHEN USING THE AXIAL PERMEAMETER

The macroscopic flow geometry is linear when the core is configured into the axial permeameter. We use a graphical approach to determine the directional permeability and  $\beta$ -factor from the experimental data. To do so, the traditional Forchheimer plot is constructed according to the one-dimensional isotropic quadratic Forchheimer equation (Eqn. (11)). The Forchheimer equation can be linearized by dividing through by the product  $\mu v$  to obtain Equation (20),

$$-\frac{1}{\mu v} \frac{d\Phi}{ds} = k_d^{-1} + \beta \frac{\rho v}{\mu} \quad (20)$$

For convenience, we use the definitions of pseudo-Reynolds number

$$\text{Pseudo-}N_{\text{Re}} = N_{\text{Rep}} = \rho v / \mu \quad (21)$$

and apparent permeability based on varying pseudo-Reynolds number (Barree & Conway, 2004),

$$k_{\text{app}}(N_{\text{Rep}}) = \frac{\mu v}{(-d\Phi/ds)}; \text{ for all pseudo-}N_{\text{Re}} \quad (22)$$

such that Equation (20) can be expressed as

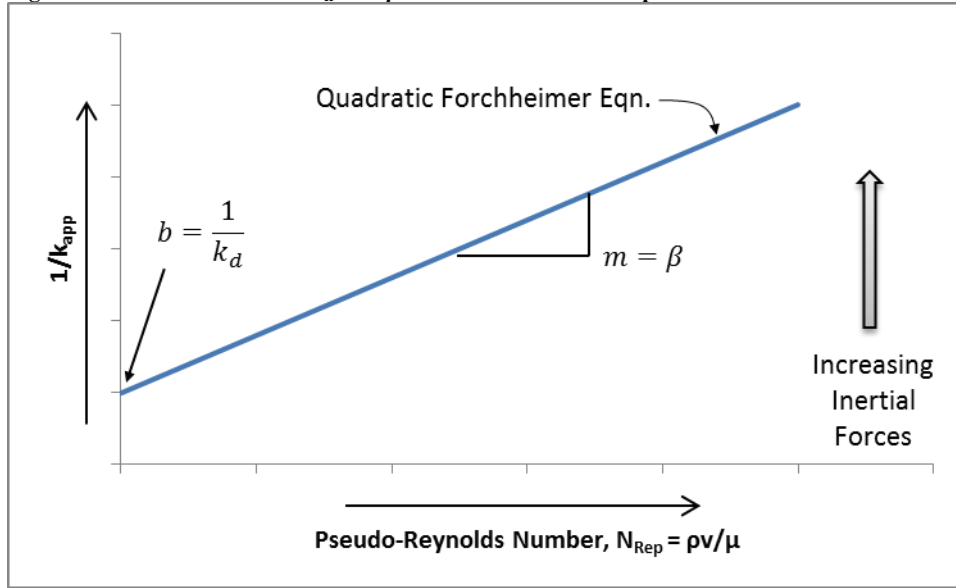
$$\underbrace{k_{\text{app}}^{-1}(N_{\text{Rep}})}_y = \underbrace{k_d^{-1}}_b + \underbrace{\beta}_{\frac{m}{\mu}} \underbrace{N_{\text{Rep}}}_x \quad (23)$$

This is a linear equation of the form  $y = mx + b$  as seen underscored in Equation (23). A plot of the reciprocal apparent permeability  $k_{\text{app}}^{-1}(N_{\text{Rep}})$  versus the pseudo-Reynolds number  $N_{\text{Rep}}$  yields a straight line with a slope equal to  $\beta$  and y-intercept equal to the reciprocal absolute Darcy permeability  $k_d^{-1}$  as shown by the blue curve in Figure 5<sup>†</sup>.

---

<sup>†</sup> The  $\beta\rho v^2$  term of Eqn. (11) states that inertial forces are always present when velocity is not zero, thus the concept of a constant value of permeability applies at the limit of zero velocity (Firoozabadi & Katz, 1979). We also note that this model for permeability determination neglects any "Pre-Darcy" and/or "threshold pressure gradient" effects (Siddiqui et al. (2015)).

Figure 5. Determination of  $k_d$  and  $\beta$  from the Forchheimer plot.



For tests flowing degassed liquids under approximately isothermal conditions and at relatively low differential pressures,  $\rho$  and  $\mu$  are approximately constant and therefore the pseudo-pressure analysis is not absolutely required. When viscous forces dominate the flow the experimental data will plot as a *nearly* horizontal line. Data exhibiting either high or low inertial effects can be evaluated using this graphical analysis technique to determine a core's axial permeability and  $\beta$ -factor, which is a more general technique than that presented in the current Section 4 manual.

The same resulting equation, Eqn (20), could be obtained starting with Eqn (19). Noting that  $A = \pi r^2$  and  $v = q/A$ , Eqn (19) can be written as

$$\Delta p = vL \left[ \frac{\mu}{k_d} + \beta \rho v^2 \right] \tag{24}$$

Dividing through by the product  $\mu v L$  gives

$$\frac{1}{\mu v} \frac{\Delta p}{L} = \frac{1}{k_d} + \beta \frac{\rho v}{\mu}; \quad \Phi \equiv p; \quad \frac{\Delta p}{L} = \int -\frac{d\Phi}{ds} \tag{25}$$

which is equivalent to Equation (20). The same procedure can be carried out on Equations (16) and (17), the results of which are listed in Table 1 below.

**Table 1. Linearized Forchheimer equations for various testing conditions for the determination of  $k_d$  and  $\beta$  (or  $k_{e\alpha}$  and  $\beta_\alpha$ ).**

Equation Valid For:	Equation used to determine $k_d$ and $\beta$ (or $k_{e\alpha}$ and $\beta_\alpha$ )	Eqn. No.
single-phase fluid, $\rho$ and $\mu$ are approximately constant	$\frac{1}{\mu v} \frac{\Delta p}{L} = \frac{1}{k_d} + \beta \frac{\rho v}{\mu};$ <p style="text-align: center;">or</p> $\frac{A\Delta p}{\mu q L} = \frac{1}{k_d} + \beta \frac{\rho q}{\mu A};$ $\Phi \equiv p$	(26)
single-phase incompressible fluid and stress apparent permeability effects	$\frac{k_{d,n}}{\bar{k}_d(\bar{p})} \frac{A\Delta m(p)}{\mu q L} = \frac{1}{k_d} + \beta \frac{\rho q}{\mu A};$ $\Phi \equiv m(p) = \frac{1}{k_{d,n}} \int_{p_b}^p k_d(p) dp + p_b$	(27)
single-phase compressible fluid	$\frac{A\Delta m(p)}{\mu_n B_n q_{sc} L} = \frac{1}{k_d} + \beta \frac{\rho_{sc} q_{sc}}{\bar{\mu} A};$ $\Phi \equiv m(p) = \mu_n B_n \int_{p_b}^p \frac{1}{\mu B} dp + p_b$	(28)
single-phase compressible fluid and stress and/or Klinkenberg apparent permeability effects	$\frac{k_{d,n}}{\bar{k}_d(\bar{p})} \frac{A\Delta m(p)}{\mu_n B_n q_{sc} L} = \frac{1}{k_d} + \beta \frac{\rho_{sc} q_{sc}}{\bar{\mu} A};$ $\Phi \equiv m(p) = \frac{\mu_n B_n}{k_{d,n}} \int_{p_b}^p \frac{k_d(p)}{\mu B} dp + p_b$	(29)
multiphase compressible fluid	$\frac{A\Delta m_\alpha(p)}{\mu_{\alpha,n} B_{\alpha,n} q_{\alpha,sc} L} = \frac{1}{k_{e\alpha}} + \beta_\alpha \frac{\rho_{\alpha,sc} q_{\alpha,sc}}{\bar{\mu}_\alpha A};$ $\Phi \equiv m_\alpha(p) = \mu_{\alpha,n} B_{\alpha,n} \int_{p_b}^p \frac{1}{\mu_\alpha B_\alpha} dp + p_b$	(30)
multiphase compressible fluid and stress and/or Klinkenberg apparent permeability effects	$\frac{k_{e\alpha,n}}{\bar{k}_{e\alpha}(\bar{p})} \frac{A\Delta m_\alpha(p)}{\mu_{\alpha,n} B_{\alpha,n} q_{\alpha,sc} L} = \frac{1}{k_{e\alpha}} + \beta_\alpha \frac{\rho_{\alpha,sc} q_{\alpha,sc}}{\bar{\mu}_\alpha A};$ $\Phi \equiv m_\alpha(p) = \frac{\mu_{\alpha,n} B_{\alpha,n}}{k_{d,n} k_{r\alpha,n}} \int_{p_b}^p \frac{k_d(p) k_{r\alpha}}{\mu_\alpha B_\alpha} dp + p_b$	(31)

The density-volumetric rate products ( $\rho q$ ) of the second terms on the right of the equations listed in Table 1 are quantitatively equivalent to mass flow rates,  $\dot{m}$ . Using these formulations in terms of mass rate avoids complications involving the varying fluid properties and maintains generality, which is useful when analyzing flow data using multiple fluid types (e.g. liquid and gas) in a single testing program.

Just like the analysis procedure for incompressible fluid flow, a plot of the left sides of Equations (26) through (31), which are equal to  $k_{app}^{-1}(N_{Rep})$  alone or a combination of  $k_{app}^{-1}(N_{Rep})$  scaled by the dimensionless ratios  $k_{r\alpha}$  and/or  $[k_{d,n}/\bar{k}_{app}(\bar{p})]$ , versus the pseudo-Reynolds number,

$$\text{Pseudo-}N_{Re} = N_{Rep} = \frac{\rho v}{\mu} = \frac{\rho q}{\mu A} = \frac{\rho q_{sc} B}{\mu A} = \frac{\rho_{sc} q_{sc}}{\mu A} = \frac{\dot{m}}{\mu A} \quad (32)$$

yields a straight line with a slope equal to  $\beta$  (or  $\beta_\alpha$ ) and y-intercept equal to the reciprocal absolute Darcy permeability  $k_d^{-1}$  (or effective Darcy permeability  $k_{e\alpha}^{-1}$ ) similar to the illustration in Figure 5.

## 9. EXAMPLE APPLICATIONS OF THE FORCHHEIMER PLOTTING METHOD FOR THE DETERMINATION OF $k_d$ AND $\beta$ WHEN USING AN AXIAL PERMEAMETER

Two examples of the Forchheimer plotting method are given for the determination of  $k_d$  and  $\beta$ , the first flowing a dry gas, the second flowing a degassed liquid. For the first example a dry gas was flowed through a Berea Sister Gray sandstone core in a progression of induced drawdown pressures while stressed under confining pressure and ambient room temperature (~70 °F to 80 °F). The nominal pressure conditions for the flow tests were 4,000 psi confining pressure and 2,000 psi pore pressure. The core is nominally 7 inches in diameter and 24 inches in length ( $L/(\sqrt{\pi}r) = 3.87 \therefore k_d \text{ measured} \cong k_v$ ). The core was cut with the rock's visibly identifiable bedding planes oriented parallel to its long axis. The nominal permeability as advertised by the rock supplier is 80-90 md (brine<sup>‡</sup>). Because of the variable nature of rock, the actual properties of the rock received can vary from the nominal values advertised. A probe permeameter (Brown & Smith, 2013) was used to estimate the absolute permeability of the actual rock being tested. Using the probe permeameter seventy-eight measurements were made producing a mean permeability of 126 md (note that these measurements are localized to a small volume of investigation, a hemispherical shaped volume with a radius of approximately 18 mm, and are subject to heterogeneities at this length scale).

After placing the core in the Section 4 testing vessel configured to apply the axial permeameter boundary conditions, four nominal pressure drops were planned and targeted for testing: 400 psi, 300 psi, 200 psi, and 100 psi. The wellbore pressure drawdown was changed to the next pressure drop once the flow rate-pressure drop relationship was stable. Figures 6A & 6B show the data collected. Figure 6A plots the measured mass flow rate and axial pressure drop. The mass flow rate (blue) is plotted on the primary y-axis and the axial pressure drop (red) is plotted on the secondary y-axis. Figure 6B contains plots of the

---

<sup>‡</sup> Permeability to liquids such as brines can be low due to liquid-clay interaction or to incomplete liquid saturation.

measured inlet and outlet (pore and wellbore, respectively) temperatures (plotted on the primary y-axis) and pressures (plotted on the secondary y-axis). Also included are the calculated mean viscosities (primary y-axis, orange) and densities (secondary y-axis, green). Both the viscosity and density values were calculated as a function of the cubic average pressure (Eqn (50) in Appendix A) and mean temperature. They have been multiplied by a factor so that the values fit in scale with the temperature or pressure data. For example, the viscosity values were multiplied by  $10^3$  and therefore a 20 cp value on the plot represents a viscosity value of 0.02 cp. Similarly, the density values were multiplied by  $10^4$  and therefore a 3,000 g/cm<sup>3</sup> value on the plot represents a density value of 0.30 g/cm<sup>3</sup>.

The data was filtered for portions exhibiting steady-state flow and then used to construct two analysis charts as shown in Figures 6C & 6D. The most basic of the two charts, Fig. 6C, is a plot of the measured mass flow rate and calculated apparent permeability as a function of the axial pressure drop (i.e. drawdown pressure). The apparent permeability was calculated in accordance with Equation (22) using the pseudo-pressure defined in Eqn. (28). Figure 6D is the traditional Forchheimer plot, used to calculate the absolute Darcy permeability  $k_d$  and coefficient of inertial resistivity  $\beta$ , which is plotted on the primary y-axis. In this plot the reciprocal of the apparent permeability is plotted against the pseudo-Reynolds number in accordance with Equation (28). The calculated permeability and coefficient of inertial resistivity for the core are noted on the plot. With these values,  $k_d$  and  $\beta$ , the contributions to the total pressure drop due to viscous and inertial forces are calculated and plotted on the secondary y-axis. The calculated permeability was 111 md, which agrees well with the mean permeability of 126 md determined from the probe permeameter measurements.

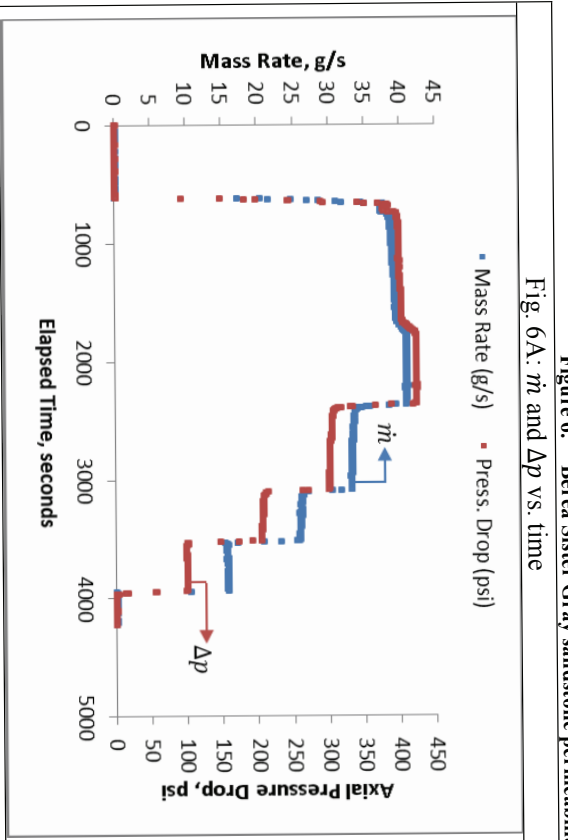


Figure 6. Berea Sister Gray sandstone permeability and  $\beta$ -factor gas flow testing data and analysis plots.

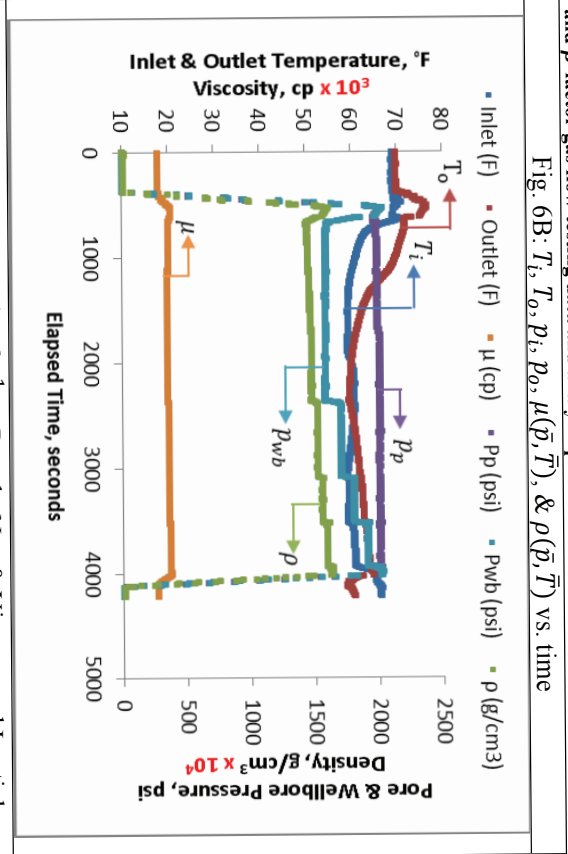


Figure 6B:  $T_i, T_o, P_i, P_o, \mu(\bar{p}, \bar{T}),$  &  $\rho(\bar{p}, \bar{T})$  vs. time

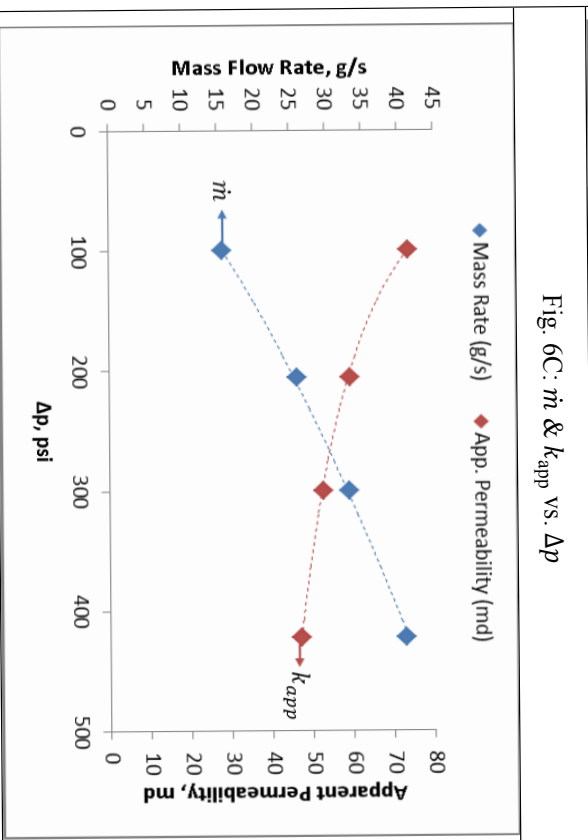


Fig. 6C:  $\dot{m}$  &  $k_{app}$  vs.  $\Delta p$

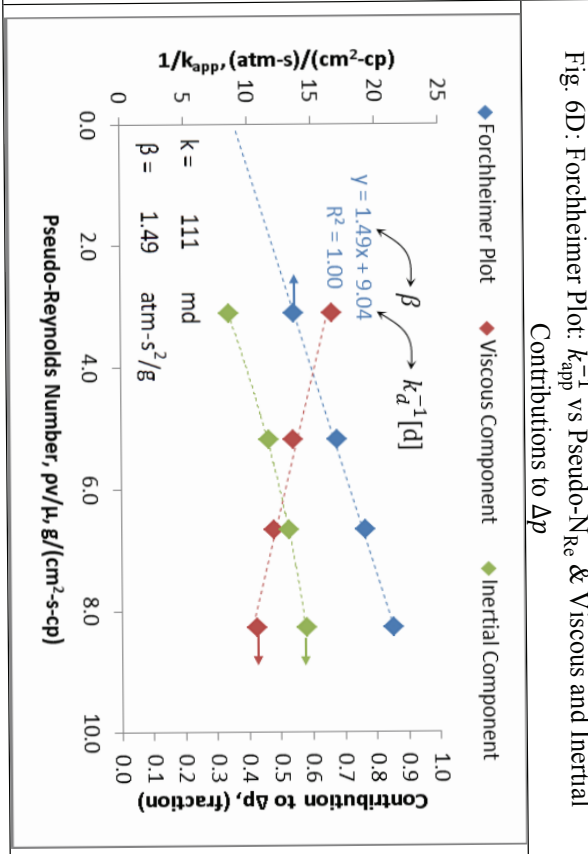
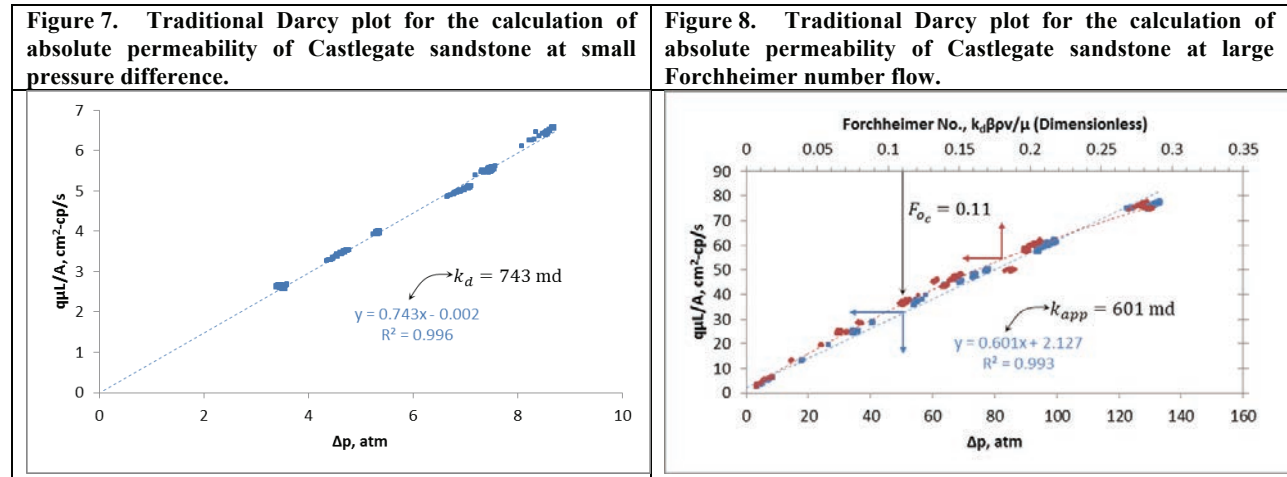


Fig. 6D: Forchheimer Plot:  $k_{app}^{-1}$  vs Pseudo- $N_{Re}$  & Viscous and Inertial Contributions to  $\Delta p$

For the second example, a Castlegate sandstone core, nominally 7 inches in diameter and 20 inches in length ( $L/(\sqrt{\pi}r) = 3.22 \therefore k_d \text{ measured} \cong k_v$ ), was flow tested with a degassed liquid as shown in Figure 9 (next page). The nominal permeability for Castlegate, as advertised by the rock supplier, ranges from 400-1,400 md (gas<sup>§</sup>). Our probe permeameter showed the core to have an absolute permeability of 751 md. Limiting the data shown in Figure 9 to  $\Delta p$ 's no greater than 130 psi, we construct the traditional Darcy plot to calculate  $k_d$  as shown in Figure 7. The slope of this data shows the permeability of this core to be 0.743 darcies (743 md), which is in good agreement with the 754 md permeability calculated and shown on the Forchheimer plot in Figure 9D, and with the mean probe permeability of 751 md. If one were to perform the same analysis including all the  $\Delta p$  data as shown in Figure 8, a  $k_d = 601$  md would be calculated, which is approximately 140 md less than the values calculated in Figure 7 and from the Forchheimer plot of Figure 9D. As shown by the red curve in Figure 8, the data exhibits Forchheimer numbers beyond the critical Forchheimer number  $F_{Oc}$  of 0.11 (as defined by Zeng & Grigg (2006)). Thus the Darcy permeability calculated is erroneous because we include data with significant inertial effects.



<sup>§</sup> Absolute Darcy permeability does not depend on the fluid type (i.e. gas or liquid) if the fluid is not chemically reactive to the minerals of the rock. Typically when gas is specified to qualify the permeability value, the permeability testing was conducted at a low mean pressure where the Knudsen-Klinkenberg (slippage) effect applies, which causes the apparent permeability to be greater than the absolute Darcy permeability (which is by definition a non-Darcy flow).

Figure 9. Castlegate sandstone permeability and  $\beta$ -factor liquid flow testing data and analysis plots.

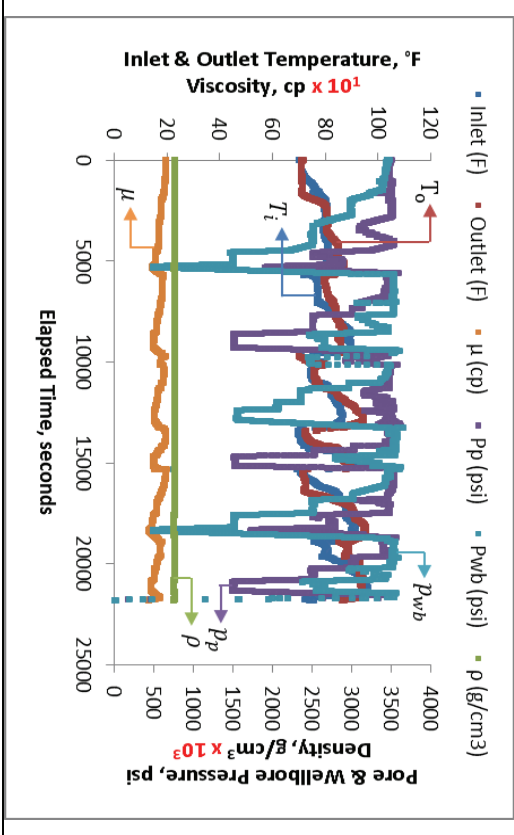
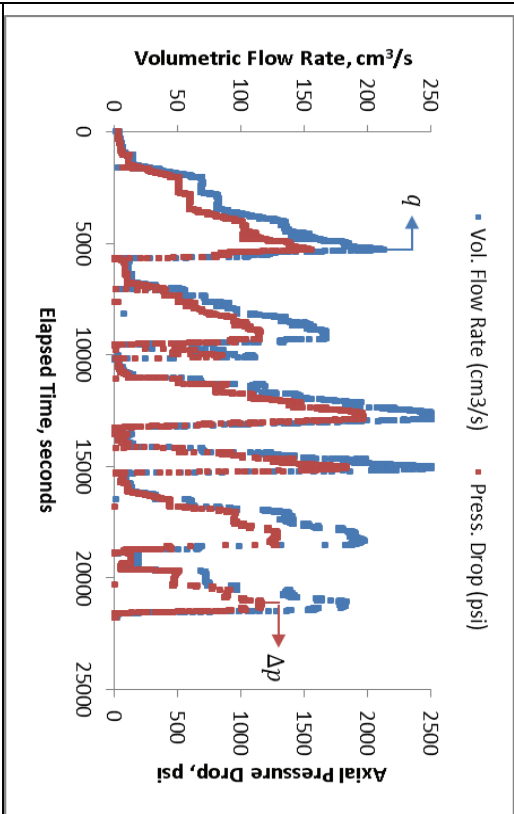


Fig. 9C:  $q$  &  $k_{app}$  vs.  $\Delta p$

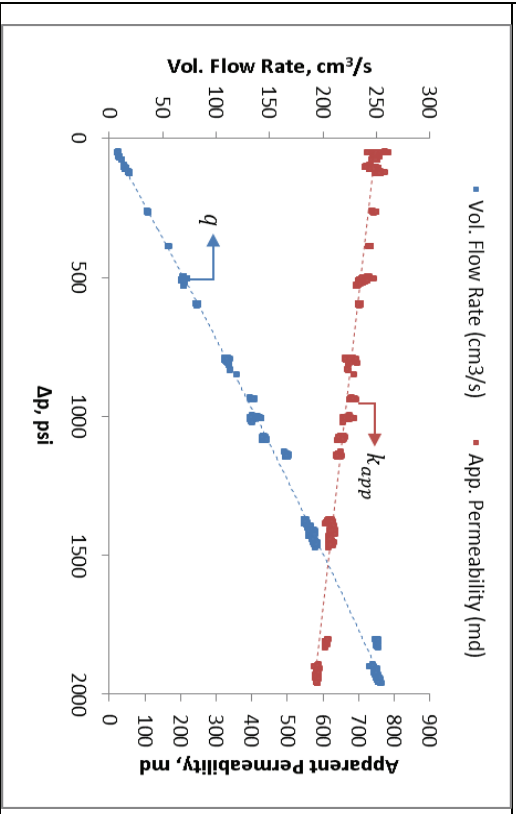
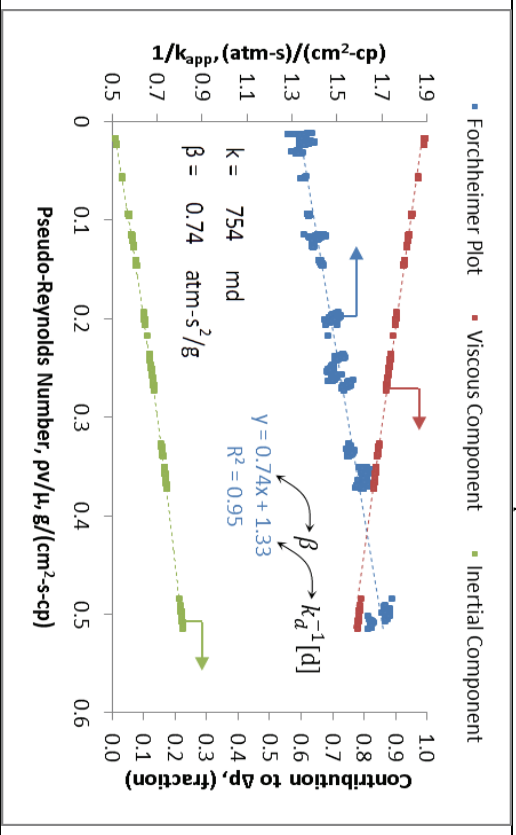


Fig. 9D: Forchheimer Plot:  $k_{app}^{-1}$  vs Pseudo- $N_{re}$  & Viscous and Inertial Contributions to  $\Delta p$



## 10. DETERMINING THE MAXIMUM AND MINIMUM DIAMETRAL DIRECTIONAL PERMEABILITY VALUES USING THE AXIAL PERMEAMETER

As mentioned in Section 5, cylindrical plugs can be cut from the whole core, transverse to the long axis of the whole core. The plugs are taken in intervals, of equal azimuthal angle  $\alpha$ , about the circumference of the core (e.g., see Johnson and Hughes (1948)) and their directional permeabilities measured using the axial permeameter. The diametral directional permeabilities and  $\beta$ -factors of the whole core can then be determined from the plugs using the same analysis procedure previously described (Sections 8 & 9). From the measured values of directional permeability  $k_d(\alpha_i)$ , which are either  $k_v$  or  $k_j$  per the plug's  $L/(\sqrt{\pi}r)$  ratio, we seek the three different components of the 2D ( $2 \times 2$ ) permeability tensor  $k_{d,ij}$  of the x-y plane which best fit these measurements. We also seek to determine the principal values (eigenvalues) and direction of the principal axes (eigenvectors) of the permeability tensor.

Using the data of Johnson and Hughes (1948), as given by Scheidegger (1954), we first plot  $\sqrt{k_d}$  and  $1/\sqrt{k_d}$  as a function of azimuthal angle in accordance to Eqns (7) & (8), respectively (Figure 10A). The plugs cut by Johnson and Hughes were no shorter or longer than 0.5 or 1.125 inches, respectively, and no greater in diameter than 0.25 inches. Thus, the minimum  $L/(\sqrt{\pi}r)$  ratio for these plugs would be 1.128; and therefore the permeabilities realized were closer to the definition given for the directional permeability in the direction of flow  $k_v$ .

It follows from the method of least squares that the best-fit ellipse to the directional permeability data can be found by solving the following system of equations if the plugs were cut at equal intervals in  $180^\circ$  (Greenkorn, Johnson, & Shallenberger, 1964; Scheidegger, 1954):

$$\begin{aligned} K_{11}\Sigma_i \cos^4 \alpha_i + K_{22}\Sigma_i \sin^2 \alpha_i \cos^2 \alpha_i &= \Sigma_i \rho_i \cos^2 \alpha_i \\ K_{11}\Sigma_i \cos^2 \alpha_i \sin^2 \alpha_i + K_{22}\Sigma_i \sin^4 \alpha_i &= \Sigma_i \rho_i \sin^2 \alpha_i \\ K_{12}\Sigma_i 2\cos^2 \alpha_i \sin^2 \alpha_i &= \Sigma_i \rho_i \cos \alpha_i \sin \alpha_i \end{aligned} \quad (33)$$

When fitting the ellipse, as given by Eqn (7),  $\rho_i$  in Eqn (33) denotes the inverse of the measured directional values  $1/k_{d,i}$  as a function of azimuth angle  $\alpha_i$ , and  $K_{11}, K_{22}, K_{12}$  are the components of the inverse permeability tensor  $1/k_{d,ij}$ . Similarly, when fitting the ellipse as given by Eqn (8),  $\rho_i$  in Eqn (33) denotes the measured directional values  $k_{d,i}$  as a function of azimuth angle  $\alpha_i$ , and  $K_{11}, K_{22}, K_{12}$  are the components of the permeability tensor  $k_{d,ij}$ . Since the permeabilities of Johnson and Hughes (1948) were measured every  $22.5^\circ$  starting with  $0^\circ$ , the solution of Eqn (33) for  $K_{11}, K_{22}, K_{12}$  is

$$\begin{aligned} K_{11} &= (3/16)\Sigma_i \rho_i \cos^2 \alpha_i - (1/16)\Sigma_i \rho_i \sin^2 \alpha_i \\ K_{22} &= (3/16)\Sigma_i \rho_i \sin^2 \alpha_i - (1/16)\Sigma_i \rho_i \cos^2 \alpha_i \\ K_{12} &= (1/4)\Sigma_i \rho_i \cos \alpha_i \sin \alpha_i \end{aligned} \quad (34)$$

---

\*\* Scheidegger (1954) erroneously gave the solution for intervals measured every  $45^\circ$  for Eqn (3.8) of his paper. Additionally, Scheidegger erroneously stated that Eqn (2.8) of his paper is an ellipsoid if the *inverse* square root of the directional permeability, Eqn (2.9) of his paper, is plotted. Eqn (2.8) of his paper is in fact an ellipsoid, however, it is an ellipsoid if the *square root* of directional permeability is plotted.

Solving for the best-fit ellipse derived for Eqn (7) using Eqn (34), the components of the inverse permeability tensor  $1/k_{d,ij}$  are found to be  $K_{11} = 0.0157, K_{22} = 0.0236,$  and  $K_{12} = -0.003 \text{ md}^{-1}$ . The normal and cross permeability coefficients are given by (Bear, 1988)

$$\bar{\bar{k}}_d = \bar{\bar{K}}^{-1} = \frac{\text{adj}(\bar{\bar{K}})}{\det(\bar{\bar{K}})} = \begin{bmatrix} 64.58 & 1.64 \\ 1.64 & 42.41 \end{bmatrix} \text{md} \quad (35)$$

The direction of the of the principal axes of  $\bar{\bar{k}}_d$ , measured counterclockwise from the designated positive x-axis, are given by (Haque, 2015)

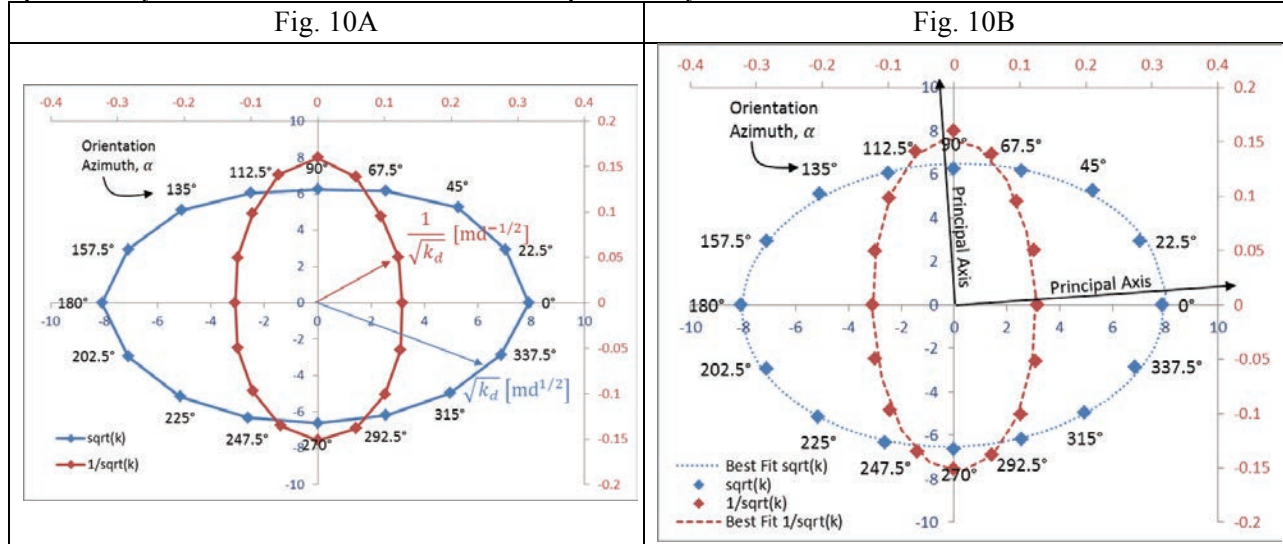
$$\begin{aligned} \theta_1 &= 0.5 \tan^{-1} [2k_{d,xy} / (k_{d,xx} - k_{d,yy})] \\ \theta_2 &= \theta_1 + 90^\circ \end{aligned} \quad (36)$$

which are found to be  $\theta_1 = 4.21^\circ, \theta_2 = 94.21^\circ$ . The principal values of the permeability tensor are found by solving the matrix eigenvalue problem; the eigenvalues  $\lambda_i (\equiv k'_{d,ii})$  are given by (Greenkorn, Johnson, & Shallenberger, 1964)

$$\lambda_i = 1/2 \left\{ k_{d,xx} + k_{d,yy} \pm \left[ (k_{d,xx} - k_{d,yy})^2 + 4k_{d,xy}^2 \right]^{1/2} \right\} \quad (37)$$

which are  $k'_{d,x} = 64.7 \text{ md}$  and  $k'_{d,y} = 42.3 \text{ md}$ , an anisotropy ratio of only  $k'_{d,y}/k'_{d,x} = 0.65$ . Using these principal permeability values and axes to draw a best fit ellipse with the measured data points, Figure 10B, the agreement is excellent.

Figure 10. (A) The actually measured directional permeability values (solid diamonds, interconnected with straight lines) plotted in accordance to the ellipses defined by Eqns (7) & (8); (B) The measured directional permeability values (solid diamonds) plotted with the ellipses defined by Eqns (7) & (8) which were calculated with the best-fitting principal permeability coefficients of the measured directional permeability values.



Solving for the best-fit ellipse derived for Eqn (8) using Eqn (34), the components of the permeability tensor  $k_{d,ij}$  are  $K_{11} = 62.19$ ,  $K_{22} = 41.64$ , and  $K_{12} = 1.45$  md, which are the normal and cross permeability coefficients. With these values, the axes positions and values of the principal permeability tensor are determined using Eqns (36) & (37), respectively, which are effectively identical to the values calculated for the best-fit ellipse derived for Eqn (7). This agreement between the two ellipses is in agreement with the sensitivity analyses of Scheidegger (1957) and Marcus and Evenson (1961) presented in Section 4. That is, the low degree of anisotropy does not necessitate that the type of directional permeability being measured,  $k_v$  or  $k_f$ , be distinguished.

To the author's knowledge, little has been published concerning the directional or tensorial nature of the Forchheimer  $\beta$ -factor. Using scalar models to propose a tensorial model for  $\beta(0)$ , it is hypothesized that if the permeability tensor is symmetric, the  $\beta$ -factor is too a symmetric 2<sup>nd</sup>-rank positive definite tensor, collinear with the permeability tensor. An effort is currently underway to better understand high-Forchheimer number flow through a point in a rock at varying directions.

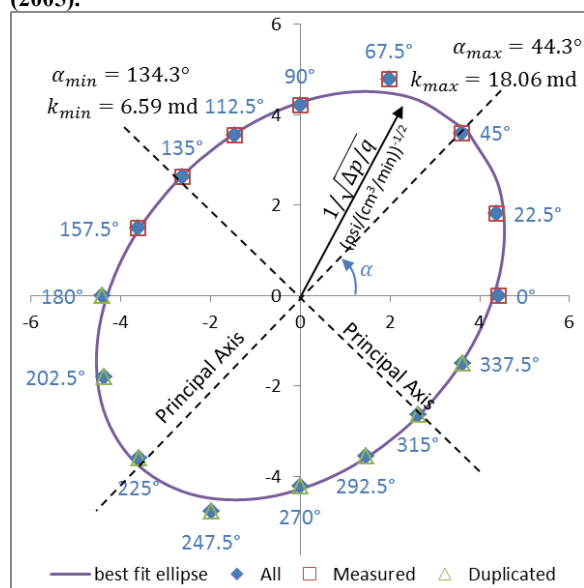
## 11. USE OF THE DIAMETRAL PERMEAMETER TO MEASURE DIRECTIONAL PERMEABILITY TRANSVERSE TO THE WHOLE CORE'S LONG AXIS

The current Section 4 manual (API, 2014) recommends that a whole-core diametral flow test be used to determine the core's principal permeability values transverse to the core's axis. The flow geometry is complex when the core is configured into the diametral permeameter (see Figure 4B). One solution for determining diametral permeability on whole core was given by Collins (1952; 1976), which assumes the core to be transversely isotropic and flow occurs across the entire length of the core's long axis, within the isotropic bedding plane. Since Collins' solution assumes isotropy, it can only provide the direction of the maximum permeability (which must be searched for) and approximate values of the maximum permeability and the permeability in the orthogonal direction (Al-Yousef, 2005).

Al-Yousef (2005) presented an analytical solution for the more general anisotropic bedding plane case, again, assuming flow occurs across the entire length of the core's long axis. Al-Yousef's solution requires a testing and analysis procedure conceptually identical to that described in Section 10. The diametral permeameter's sleeve is rotated in intervals, of equal azimuthal angle  $\alpha$ , about the circumference of the core where measurements are made. Using the reciprocal rate index  $(\Delta p/q)$  measured at each angle, the best-fit ellipse to the reciprocal rate indices are found by solving the system of equations given in Eqn (33), where  $(\Delta p/q)_{11}$ ,  $(\Delta p/q)_{22}$ , and  $(\Delta p/q)_{12}$  are used in place of  $K_{11}$ ,  $K_{22}$ , and  $K_{12}$ , respectively, and  $\rho_i = (\Delta p/q)_i$  measured at angle  $\alpha_i$ . With  $(\Delta p/q)_{11}$ ,  $(\Delta p/q)_{22}$ , and  $(\Delta p/q)_{12}$  solved for, the principle permeability values and their directions are then calculated using the equations given in Al-Yousef's (2005) paper.

The permeabilities calculated are considered directional permeabilities in the direction of the potential gradient when using the diametral permeameter (Greenkorn, Johnson, & Shallenberger, 1964; Parsons, 1964; Al-Yousef, 2005). Therefore, when presenting the data graphically, a plot of  $1/\sqrt{\Delta p/q}$  as a function of azimuthal angle in accordance with Eqn (8) is appropriate (Figure 11).

Figure 11. Plot of  $1/\sqrt{\Delta p/q}$  as a function of azimuthal angle using the data associated with "Core #1" given in Al-Yousef (2005).



Prior to Al-Yousef's anisotropic solution, Dogulu & Halleck et al. (1995; 1997) numerically simulated the error that occurs using Collins' solution when the flow measurement is performed using a modified diametral permeameter (Figure 12), where flow is along only a portion of the core length and bedding planes either run parallel or perpendicular to the long axis of the core. In this scenario some flow penetrates beyond the test region (below the screen), causing an overestimation of diametral permeability by an amount that depends on the magnitude of permeability anisotropy, core size, and bedding plane orientation. Their investigation assumed that the permeability is isotropic within the bedding planes. Based on their numerical simulations, they presented a series of four graphs containing correction factors  $F$  for cores having varying length-to-radius dimensions ( $L/r = 4, 5, 6,$  and  $10$ ). Within each graph are five curves representing the different partial flow length-to-core length ratios tested ( $L_i/L = 0.3, 0.4, 0.5, 0.6,$  and  $0.7$ ), where the cross-diameter flow correction factor  $F$  is plotted as a function of diametral-to-axial

permeability anisotropy ratios ranging between 0.01 and 100. The lower anisotropy ratios (0.01 - 1.0) were calculated using cores with bedding planes parallel to the axis of the core, the higher ratios (1.0 - 100) with bedding planes perpendicular to the core's axis.

The Section 4 manual provides a single equation, Eqn. 4-6 of API (2014), for the cross-diameter flow correction factor that is specific to a core size having a length-to-radius ratio of 5.14 and partial flow length-to-core length ratio of 0.67:

$$F = 1.232 - 0.2371 \tanh \left[ \frac{0.7162 \log k_{\text{dia}}}{k_{\text{axi}}} + 0.612 \right] \tag{38}$$

This equation was developed for conditions that most closely match the bottom curve ( $L_i/L = 0.7$ ) of Figure 5 given in Halleck & Dogulu et al. (1997), shown here (Figure 13) with the bottom curve highlighted yellow. Plotting values for  $F$  using Eqn. (38) as written results in the blue curve as shown on Figure 13. Because of the lack of agreement between the yellow and blue curves, Eqn. (38) was modified by including the axial permeability  $k_{\text{axi}}$  term in the logarithm function as shown in Eqn. (39), which produces  $F$  values (red curve) that are in better agreement with the yellow curve.

$$F = 1.232 - 0.2371 \tanh[0.7162 \log(k_{\text{dia}}/k_{\text{axi}}) + 0.612] \tag{39}$$

Figure 12. Boundary conditions for modified diametral flow in the modified diametral permeameter.

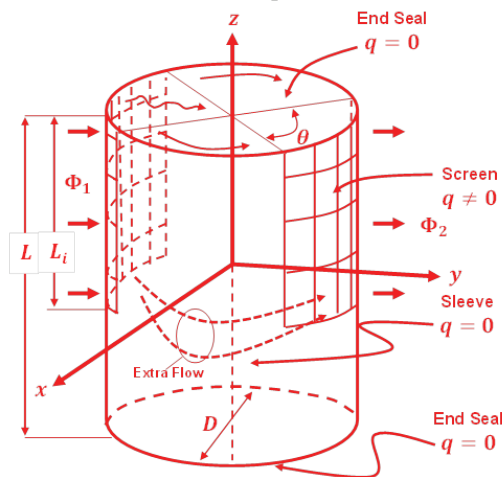
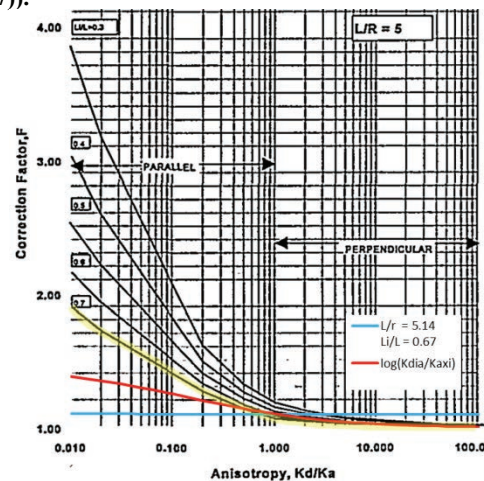


Figure 13. Correction factors for samples with  $L/r = 5$  (modified and sourced from Dogulu & Halleck et al. (1997)).



---

## CONCLUDING REMARKS

An analysis procedure has been presented for the determination of a core's axial and diametral absolute (or effective to phase  $\alpha$ ) permeabilities and  $\beta$ -factors. The procedure works for both gases and liquids flowed at both high and low Forchheimer numbers.

Convenient formulations of the quadratic Forchheimer equation have been presented for various flow geometries and account for various effects such as the presence of multiple fluid phases and changing rock and fluid properties as a function of pressure.

The methods used to determine a core's diametral Darcy permeabilities were introduced, and examples are given on how to determine a core's principal permeabilities and axes of anisotropy in its transverse plane.

A tensorial model for  $\beta$ , developed using scalar models for  $k_d$  and  $\beta$ , was given in support of the hypothesis that if the permeability tensor is symmetric, the Forchheimer  $\beta$ -factor is too a symmetric 2<sup>nd</sup>-rank positive definite tensor, collinear with the permeability tensor.

It will be shown in the second part of the article how these formulations are relevant to analyzing post-shot flow.

.....

## NOMENCLATURE

<u>English</u>	<u>Definition</u>	<u>Dimension</u>	<u>Units used in Equations</u>
$a$	= dimensional constant = $2.75 \times 10^{19}$ d/cm	L	d/cm
$A$	= bulk cross-sectional area normal to macroscopic direction of flow	$L^2$	$cm^2$
$B$	= formation volume factor	$L^3/L^3$	$R.cm^3/S.cm^3$ [Rsvr vol./Srvc vol.]
$c$	= empirical numerical factor	-	-
$D$	= diameter, core diameter	L	cm
$\bar{D}$	= the square root of the inverse of the permeability tensor	$L^{-1/2}$	$d^{-1/2}$
$F$	= Diametral permeability correction factor for the modified diametral permeameter (Figure 12)	-	-
$F_o$	= Forchheimer number, $F_o = k_d \beta \rho v / \mu = k_d \beta \dot{m} / \mu$ , a macroscopic Reynolds number, where $k_d \beta$ is considered the characteristic length of the porous medium. It represents the ratio of fluid energy consumed by fluid-solid interactions to that by viscous resistance.	-	-
$g$	= gravitational acceleration, $\cong 9.81$ m/s <sup>2</sup>	$L/t^2$	m/s <sup>2</sup>
$\vec{J}$	= fluid potential gradient vector ( $\equiv -\nabla\Phi$ )	$M/L^2t^2$	atm/cm
$k_{app}$	= apparent permeability	$L^2$	d
$k_{axi}$	= the axial direction permeability value to be used in Eqn (38), which is Eqn. 4-6 of API (2014)	$L^2$	md
$k_b$	= the base permeability used to define $k_{r\alpha}$	$L^2$	d
$k_d$	= absolute Darcy permeability	$L^2$	d
$k_{dia}$	= the diametral direction permeability value to be used in Eqn (38), which is Eqn. 4-6 of API (2014)	$L^2$	md
$k_{d,ij}$	= absolute Darcy permeability coefficient in the $i$ direction due to the potential gradient in the $j$ direction	$L^2$	d
$k'_{d,i}$	= principal absolute Darcy permeability coefficient in the $i$ direction ( $x, y, z$ )	$L^2$	d
$k_{e\alpha}$	= effective permeability to phase $\alpha$	$L^2$	d
$k_J$	= the directional permeability in the direction of the gradient	$L^2$	d
$k_{r\alpha}$	= relative permeability to phase $\alpha$ ( $= k_{e\alpha}/k_b$ )	$L^2/L^2$	fraction
$k_v$	= the directional permeability in the direction of flow	$L^2$	d
$\bar{\bar{k}}_d$	= absolute Darcy permeability tensor	$L^2$	d
$\bar{\bar{k}}'_d$	= principal absolute Darcy permeability tensor	$L^2$	d
$K_{ii}$	= Defined for Eqn (33), $K_{ii}$ can take on two different values depending on which permeability tensor ellipse it is being used to model. When fitting the tensor ellipse as given by Eqn (7), $K_{ii}$ denotes the components of the inverse permeability tensor $1/k_{d,i}$ . When fitting the tensor ellipse as given by Eqn (8), $K_{ii}$ denotes the components of the permeability tensor $k_{d,i}$ .	$L^{-2}$ or $L^2$	$d^{-1}$ or d

$\bar{\mathbf{K}}$	= the inverse of the permeability tensor	$L^{-2}$	$d^{-2}$
$L$	= length, core length	$L$	cm
$L_e$	= total length fluid travels through the tortuous pathways in the porous medium	$L$	cm
$L_i$	= partial sample length over which permeability is measured in the modified diametral permeameter	$L$	cm
$m(p)$	= pseudo-pressure	$M/Lt^2$	atm
$\dot{m}$	= mass rate	$M/t$	g/s
$N_{Rep}$	= Pseudo-Reynolds number $\equiv \rho v/\mu$	-	-
$p$	= pressure	$M/Lt^2$	atm
$q$	= volumetric flow rate	$L^3/t$	$cm^3/s$
$r$	= radius, core radius	$L$	cm
$s$	= distance in the direction of flow, which is always taken as positive	$L$	cm
$S_p$	= the wetted surface area of the pore per unit pore volume of the porous medium	$L^2/L^2$	fraction
$v$	= superficial "Darcy" velocity (also referred to as volumetric flux, specific discharge, etc.)	$L/t$	cm/s
$z$	= height above (or below) an arbitrary datum	$L$	cm

<u>Greek</u>	<u>Definition</u>	<u>Dimension</u>	<u>Units</u>
$\alpha$	= azimuthal angle	-	rad or °
$\alpha_x, \alpha_y, \alpha_z$	= the angles between $\vec{\mathbf{j}}$ and the three principal axes, $x, y,$ and $z,$ respectively	-	rad or °
$\beta_x, \beta_y, \beta_z$	= the angles between $\vec{\mathbf{v}}$ and the three principal axes, $x, y,$ and $z,$ respectively	-	rad or °
$\beta, \bar{\beta}$	= beta-factor, beta-factor tensor	$1/L$	$atm \cdot s^2/g$
$\theta$	= the angle between the vectors $\vec{\mathbf{v}}$ (components $v_x, v_y, v_z$ ) and $\vec{\mathbf{j}}$ (components: $J_x, J_y, J_z$ )	-	rad or °
$\theta$	= the angle that the "screens" of the diametral permeameter subtend	-	rad or °
$\theta^{\circ}_i$	= the angular direction of one of the principal permeability coefficients	-	rad or °
$\lambda_i$	= Eigenvalues of permeability tensor	$L^2$	d
$\mu$	= dynamic viscosity	$M/Lt$	cp
$\pi$	= transcendental number, 'pi', 3.1415...	-	-
$\rho$	= volumetric mass density	$M/L^3$	$g/cm^3$
$\rho_i$	= Defined for Eqn (33), $\rho_i$ can take on two different values depending on which permeability tensor ellipse it is being used to model. When fitting the tensor ellipse as given by Eqn (7), $\rho_i$ denotes the inverse of the measured directional values $1/k_{d,i}$ . When fitting the tensor ellipse as given by Eqn (8), $\rho_i$ denotes the measured directional values $k_{d,i}$ .	$L^{-2}$ or $L^2$	$d^{-1}$ or d
$\tau$	= tortuosity of porous media	-	-
$\phi$	= porosity	$L^3/L^3$	fraction
$\Phi$	= fluid potential	$M/Lt^2$	atm

<u>Subscript</u>	<u>Definition</u>
$b$	= base (pressure) or defined base permeability
$c$	= critical (Forchheimer number $F_o$ )
$d$	= to denote "Darcy"
$e$	= "effective" or "effective to"
$i, j$	= dummy indices
$o$	= an arbitrarily or conveniently selected reference, datum, or base level
$n$	= normalizing (variable is evaluated at a normalizing pressure and temperature)
$x$	= x-direction coordinate
$y$	= y-direction coordinate
$z$	= z-direction coordinate
$sc$	= standard surface condition, defined as 60 °F and 14.65 psia in Texas, USA
$\alpha$	= fluid phase, including oil ( $o$ ), water ( $w$ ), gas ( $g$ ), and so on

<u>Math Symbol</u>	<u>Definition (z is used as a dummy variable for definitions)</u>
$\Delta$	= finite difference operator or incremental change in a variable, e.g., $\Delta z = z_1 - z_2$
$\nabla$	= gradient operator, $\nabla \equiv \frac{\partial}{\partial x} \mathbf{i} + \frac{\partial}{\partial y} \mathbf{j} + \frac{\partial}{\partial z} \mathbf{k}$ , where $\mathbf{i}, \mathbf{j}, \mathbf{k}$ are unit vectors in the $x, y, z$ directions, respectively
$\Sigma_i$	= summation over indices $i$ , $\Sigma_i z_i = z_1 + z_2 + \dots + z_n$
$\int_{z_1}^{z_2} z \, dz$	= the integral taken between the values of $z_1$ and $z_2$ of the variable $z$
$\leq$	= less than or equal to
$\equiv$	= is identical to or defined by
$\rightarrow$	= tends to
$\therefore$	= therefore
$\dot{z}$	= rate of change of variable $z$ with respect to time
$\bar{z}$	= average value of variable $z$
$\vec{z}$	= vector notation for variable $z$
$\bar{\bar{z}}$	= 2 <sup>nd</sup> -rank tensor notation for variable $z$
$ \vec{z} $	= the $l^2$ -norm or magnitude of the vector $\vec{z} = \sqrt{z_x^2 + z_y^2 + z_z^2}$
$\frac{d}{dz}$	= ordinary derivative operator with respect to $z$
$\frac{\partial}{\partial z}$	= partial derivative operator with respect to $z$
$\text{adj}(\bar{\bar{z}})$	= the adjugate of $\bar{\bar{z}}$ .
$\text{det}(\bar{\bar{z}})$	= the determinant of $\bar{\bar{z}}$ .

**Appendix A. Derivation of the Integrated Quadratic Forchheimer Equation Using a Pseudo-Pressure Accounting for the Presence of Multiple Fluid Phases and Changing Rock and Fluid Properties as a Function of Pressure**

Using Equation (15) as the definition of pseudo-pressure, its derivative with respect to position  $s$  is

$$\frac{\partial m_\alpha(p)}{\partial s} = \frac{\partial m_\alpha(p)}{\partial p} \cdot \frac{\partial p}{\partial s} = \frac{\mu_{\alpha,n} B_{\alpha,n}}{k_{d,n} k_{r\alpha,n}} \cdot \frac{k_d k_{r\alpha}}{\mu_\alpha B_\alpha} \cdot \frac{\partial p}{\partial s} \quad (40)$$

Therefore, equating Equation (40) with Equation (11) (including  $k_{r\alpha}$  and  $\beta_\alpha$ ) gives

$$\frac{\partial m_\alpha(p)}{\partial s} = - \frac{\mu_{\alpha,n} B_{\alpha,n}}{k_{d,n} k_{r\alpha,n}} \cdot \frac{k_d k_{r\alpha}}{\mu_\alpha B_\alpha} \cdot \left[ \frac{\mu_\alpha}{k_d k_{r\alpha}} v_\alpha + \beta_\alpha \rho_\alpha v_\alpha^2 \right] \quad (41)$$

Distributing the product  $\frac{\mu_{\alpha,n} B_{\alpha,n}}{k_{d,n} k_{r\alpha,n}} \cdot \frac{k_d k_{r\alpha}}{\mu_\alpha B_\alpha}$  gives

$$- \frac{\partial m_\alpha(p)}{\partial s} = \frac{\mu_{\alpha,n} B_{\alpha,n}}{k_{d,n} k_{r\alpha,n}} \cdot \frac{k_d k_{r\alpha}}{\mu_\alpha B_\alpha} \cdot \frac{\mu_\alpha}{k_d k_{r\alpha}} v_\alpha + \frac{\mu_{\alpha,n} B_{\alpha,n}}{k_{d,n} k_{r\alpha,n}} \cdot \frac{k_d k_{r\alpha}}{\mu_\alpha B_\alpha} \cdot \beta_\alpha \rho_\alpha v_\alpha^2 \quad (42)$$

Noting that  $k_d k_{r\alpha} = k_{e\alpha}$ , Eqn. (42) can be written as

$$- \frac{\partial m_\alpha(p)}{\partial s} = \frac{\mu_{\alpha,n} B_{\alpha,n}}{k_{e\alpha,n}} \cdot \frac{k_{e\alpha}(p)}{\mu_\alpha B_\alpha} \cdot \frac{\mu_\alpha}{k_{e\alpha}} v_\alpha + \frac{\mu_{\alpha,n} B_{\alpha,n}}{k_{e\alpha,n}} \cdot \frac{k_{e\alpha}(p)}{\mu_\alpha B_\alpha} \cdot \beta_\alpha \rho_\alpha v_\alpha^2 \quad (43)$$

Invoking the relations  $\dot{m}_\alpha / \rho_\alpha = A v_\alpha = q_\alpha$  and  $B_\alpha = \rho_{\alpha,sc} / \rho_\alpha$  (the general formation volume factor for dry gas and undersaturated liquid) into Equation (43), and noting that  $\rho_\alpha q_\alpha = \rho_{\alpha,sc} q_{\alpha,sc}$ , yields:

$$- \frac{\partial m_\alpha(p)}{\partial s} = \frac{\mu_{\alpha,n} B_{\alpha,n}}{k_{e\alpha,n}} \cdot \frac{k_{e\alpha}(p)}{k_{e\alpha}} \cdot \frac{q_{\alpha,sc}}{A} + \frac{\mu_{\alpha,n} B_{\alpha,n}}{k_{e\alpha,n}} \cdot \frac{k_{e\alpha}(p)}{\mu_\alpha} \cdot \beta_\alpha \rho_{\alpha,sc} \cdot \frac{q_{\alpha,sc}^2}{A^2} \quad (44)$$

Equation (44) may be integrated with respect to the geometry through which the fluid flows and by taking the direction of the fluid flow with respect to the coordinate system into consideration. The equations listed in Figure 14 give the cross-sectional areas normal to flow for linear, radial, and hemispherical geometries, along with the sign of the potential gradient with respect to the coordinate system and flow direction.

Figure 14. Flow geometries and their equations for cross-sectional area normal to flow.

Geometry	Linear	Radial	Hemispherical
Visual Rep.			
CSA*	$A = \pi r^2$	$A = 2\pi rL$	$A = 2\pi r^2$
Eqn. No.	(45)	(46)	(47)

\*CSA = Cross-sectional area normal to flow.

Using the linear flow geometry for positive direction flow as an example, Equation (44) is integrated as follows:

$$-\int_{m_\alpha(p_1)}^{m_\alpha(p_2)} \partial m_\alpha(p) = \frac{\mu_{\alpha,n} B_{\alpha,n}}{k_{e\alpha,n}} \cdot \frac{q_{\alpha,sc}}{\pi r^2 k_{e\alpha}} \cdot \int_{x_1}^{x_2} k_{e\alpha}(p) \partial x + \frac{\mu_{\alpha,n} B_{\alpha,n}}{k_{e\alpha,n}} \cdot \frac{\beta_\alpha \rho_{\alpha,sc} q_{\alpha,sc}^2}{\pi^2 r^4} \int_{x_1}^{x_2} \frac{k_{e\alpha}(p)}{\mu_\alpha} \partial x \quad (48)$$

which upon integration the following expression is obtained

$$\Delta m_\alpha(p) = \frac{\mu_{\alpha,n} B_{\alpha,n} \bar{k}_{e\alpha}(\bar{p})}{k_{e\alpha,n}} \cdot \frac{q_{\alpha,sc}}{\pi r^2 k_{e\alpha}} L + \frac{\mu_{\alpha,n} B_{\alpha,n} \bar{k}_{e\alpha}(\bar{p})}{k_{e\alpha,n}} \cdot \frac{\beta_\alpha \rho_{\alpha,sc} q_{\alpha,sc}^2}{\pi^2 r^4 \bar{\mu}_\alpha} L \quad (49)$$

$$\Delta m_\alpha(p) = m_\alpha(p_1) - m_\alpha(p_2)$$

We note that in order to evaluate the integral for the first term on the right-hand side of Equation (48), the stress/pressure-dependent effective permeability term  $k_{e\alpha}(p)$  was pulled from the integral and approximated using an evaluation pressure, taken here as the cubic average pressure  $\bar{p}$  (Chalmers, Taliaferro, & Rawlins, 1932),

$$\bar{p} = \frac{2(p_i^3 - p_o^3)}{3(p_i^2 - p_o^2)} = \frac{2}{3} \left( p_i + p_o - \frac{p_i p_o}{p_i + p_o} \right) \quad (50)$$

Likewise, for the second term on the right-hand side of Equation (48), the viscosity term  $\mu_\alpha$ , along with  $k_{e\alpha}(p)$ , was pulled from the integral and approximated using the evaluation pressure  $\bar{p}$ . Equation (49) is a simplified integral form of Equation (44), as it can only be integrated numerically. Equation (49) may be simplified by factoring like terms

$$\Delta m_{\alpha}(p) = \frac{\mu_{\alpha,n} B_{\alpha,n} \bar{k}_{e\alpha}(\bar{p})}{k_{e\alpha,n}} \cdot \frac{q_{\alpha,sc} L}{\pi r^2} \left[ \frac{1}{k_{e\alpha}} + \frac{\beta_{\alpha} \rho_{\alpha,sc} q_{\alpha,sc}}{\pi r^2 \bar{\mu}_{\alpha}} \right] \quad (51)$$

The same integration procedure can be performed for other flow geometries and flow directions.

For reference, Table 2 below lists the Forchheimer equation, Equation (44), integrated for linear, radial, and hemispherical flow geometries. The radial and hemispherical flow geometries are relevant for post-shot flow performance; the relevance of which will be developed further in the second part of the article. The differential fluid potentials in Table 2 are defined as follows:

Production Direction Flow	Injection Direction Flow
$\Delta\Phi = m_{\alpha}(p_2) - m_{\alpha}(p_1) > 0$	$\Delta\Phi = m_{\alpha}(p_1) - m_{\alpha}(p_2) > 0$

**Table 2. Integrated Forchheimer equations, assuming stress and/or Klinkenberg apparent permeability effects and compressible multiphase flow, for linear, radial, and hemispherical geometries.**

Flow Geometry	Integrated Forchheimer Equation	Eqn. No.
Linear	$\Delta m_{\alpha}(p) = \frac{\mu_{\alpha,n} B_{\alpha,n} \bar{k}_{e\alpha}(\bar{p})}{k_{e\alpha,n}} \cdot \frac{q_{\alpha,sc} L}{\pi r^2} \left[ \frac{1}{k_{e\alpha}} + \frac{\beta_{\alpha} \rho_{\alpha,sc} q_{\alpha,sc}}{\pi r^2 \bar{\mu}_{\alpha}} \right]$	(52)
Radial	$\Delta m_{\alpha}(p) = \frac{\mu_{\alpha,n} B_{\alpha,n} \bar{k}_{e\alpha}(\bar{p})}{k_{e\alpha,n}} \cdot \frac{q_{\alpha,sc}}{2\pi L} \left[ \frac{1}{k_{e\alpha}} \ln \left( \frac{r_2}{r_1} \right) + \frac{\beta_{\alpha} \rho_{\alpha,sc} q_{\alpha,sc}}{2\pi L \bar{\mu}_{\alpha}} \left( \frac{1}{r_1} - \frac{1}{r_2} \right) \right]$	(53)
Hemi-spherical	$\Delta m_{\alpha}(p) = \frac{\mu_{\alpha,n} B_{\alpha,n} \bar{k}_{e\alpha}(\bar{p})}{k_{e\alpha,n}} \cdot \frac{q_{\alpha,sc}}{2\pi} \left[ \frac{1}{k_{e\alpha}} \left( \frac{1}{r_1} - \frac{1}{r_2} \right) + \frac{\beta_{\alpha} \rho_{\alpha,sc} q_{\alpha,sc}}{2\pi \bar{\mu}_{\alpha}} \left( \frac{1}{3r_1^3} - \frac{1}{3r_2^3} \right) \right]$	(54)

### Appendix B. A Tensorial Model of the Forchheimer $\beta$ -Factor

To make a connection between the permeability tensor and the  $\beta$ -factor, we make use of both the one-dimensional Kozeny-Carman equation (Peters, 2012)

$$k_d = \frac{\phi}{c\tau^2 S_p^2}; \quad \tau = L_e/L \quad (55)$$

and the experimentally derived one-dimensional relationship between  $k$  and  $\beta$  found by Liu et al. (1995),

$$\beta = \frac{a\tau}{k_d\phi} \quad (56)$$

Rearranging Eqn (55) to solve for tortuosity  $\tau$

$$\tau = \frac{\phi^{1/2}}{c^{1/2}k_d^{1/2}S_p} \quad (57)$$

and then substituting this equation into Eqn (56), we obtain

$$\beta = \frac{a}{c^{1/2}\phi^{1/2}k_d^{1/2}kS_p} \quad (58)$$

Defining a scalar constant  $C = a/(c^{1/2}\phi^{1/2}S_p)$  for simplification ( $a, c, \phi, & S_p$  are all scalar quantities), Eqn (58) is now written as

$$\beta = \frac{C}{k_d^{1/2}k_d} \quad (59)$$

To write Eqn (59) in tensorial form, denote the inverse of the permeability tensor as:  $\bar{k}_d^{-1} = \bar{K}$  and denote the square root of the inverse of the permeability tensor as:  $\bar{K}^{1/2} = \bar{D}$  where  $\bar{D} \cdot \bar{D} = \bar{K}$ . Accordingly, Eqn (59) is now written, taking  $C = 1$  for simplicity, as either:

$$\bar{\beta} = \bar{D} \cdot \bar{K} \quad (60)$$

or

$$\bar{\beta} = \bar{K} \cdot \bar{D} \quad (61)$$

since in general multiplication of matrices is not commutative.

To apply numerical values and see how the above derivation might work, permeability coefficients were assigned to the 3 x 3 matrix of the permeability tensor:

$$\bar{k}_d [d] = \begin{bmatrix} 200 & 50 & 40 \\ 50 & 150 & 30 \\ 40 & 30 & 100 \end{bmatrix} \quad (62)$$

To verify that the permeability matrix is symmetrical and positive definite, the eigenvalues of the permeability matrix,  $\bar{\bar{K}}'_{d,ii}$ , are (rounding): 82.71, 119.58, and 247.71 darcies, which are all positive eigenvalues. This affirms that the permeability tensor is symmetric and positive definite.

The inverse of the permeability matrix (Eqn (62)) is,

$$\bar{\bar{K}} [d^{-1}] = \begin{bmatrix} 0.0058 & -0.0016 & -0.0018 \\ -0.0016 & 0.0075 & -0.0016 \\ -0.0018 & -0.0016 & 0.0112 \end{bmatrix} \quad (63)$$

And the square root of the inverse permeability matrix is,

$$\bar{\bar{D}} [d^{-1/2}] = \begin{bmatrix} 0.0744 & -0.0103 & -0.0108 \\ -0.0103 & 0.0856 & -0.0092 \\ -0.0108 & -0.0092 & 0.1050 \end{bmatrix} \quad (64)$$

Performing the calculation of Eqn (60), we obtain:

$$\bar{\bar{\beta}} [\text{atm-s}^2/\text{g}] = \begin{bmatrix} 0.0005 & -0.0002 & -0.0002 \\ -0.0002 & 0.0007 & -0.0002 \\ -0.0002 & -0.0002 & 0.0012 \end{bmatrix} \quad (65)$$

which is symmetrical. The eigenvalues,  $\bar{\bar{\beta}}'_{ii}$ , of Eqn (65) are all positive: 0.0003, 0.0008, and 0.0013 atm-s<sup>2</sup>/g, thus this  $\bar{\bar{\beta}}$ -factor tensor is symmetric and positive definite. Performing the calculation of Eqn (61), we obtain:

$$\bar{\bar{\beta}} [\text{atm-s}^2/\text{g}] = \begin{bmatrix} 0.0005 & -0.0002 & -0.0002 \\ -0.0002 & 0.0007 & -0.0002 \\ -0.0002 & -0.0002 & 0.0012 \end{bmatrix} \quad (66)$$

which is equivalent to Eqn (65). Thus, for this instance the multiplication of the matrices  $\bar{\bar{K}}$  and  $\bar{\bar{D}}$  as they are defined is commutative. Based on these results, it is hypothesized that, if the Darcy permeability tensor is symmetric, the Forchheimer  $\beta$ -factor is too a symmetric 2<sup>nd</sup>-rank positive definite tensor that is collinear with the Darcy permeability tensor.

---

 WORKS CITED

- Al-Hussainy, R., Ramey, H. J., & Crawford, P. B. (1966, May). The Flow of Real Gases Through Porous Media. *Society of Petroleum Engineers*. doi:10.2118/1243-A-PA
- Al-Yousef, H. Y. (2005). Permeability Anisotropy Measurement on Whole Cores--Analytical Solution and Application. Society of Petroleum Engineers. doi:10.2118/93559-MS
- Ames, W. F., & Ames, R. (1965). *Nonlinear Partial Differential Equations in Engineering*. Elsevier Science.
- API. (1998). *Recommended Practices for Core Analysis* (2nd ed.). American Petroleum Institute.
- API. (2014). *Recommended Practices for Evaluation of Well Perforators* (2nd Ed. Sep. 2006; Re'Affd 2011; Addnded 2014 ed.). American Petroleum Institute.
- Barree, R. D., & Conway, M. W. (2004). Beyond Beta Factors: A Complete Model for Darcy, Forchheimer, and Trans-Forchheimer Flow in Porous Media. *Society of Petroleum Engineers*. doi:10.2118/89325-MS
- Bear, J. (1988). *Dynamics of Fluids in Porous Media*. New York: Dover Publications, Inc.
- Bear, J., & Cheng, A. H.-D. (2010). *Modeling Groundwater Flow and Contaminant Transport*. Springer. doi:10.1007/978-1-4020-6682-5
- Brown, S., & Smith, M. (2013, September-October). A transient-flow syringe air permeameter. *GEOPHYSICS*, 78(5), D307-D313. doi:10.1190/GEO2012-0534.1
- Caldwell, J. A. (1971). *The Theoretical Determination Of The Fluid Potential Distribution In Jointed Rocks*. University of the Witwatersrand. University of the Witwatersrand, Johannesburg.
- Carslaw, H. S., & Jaeger, J. C. (1959). *Conduction of heat in solids*. Oxford: Clarendon Press.
- Chalmers, J., Taliaferro, D., & Rawlins, E. (1932). Flow of Air and Gas through Porous Media. SPE 932375-G. doi:10.2118/932375-G
- Civan, F. (2011). *Porous Media Transport Phenomena*. Hoboken, New Jersey: John Wiley & Sons.
- Collins, R. E. (1952, June). Determination of Transverse Permeabilities of Large Core Samples from Petroleum Reservoirs. *Journal of Applied Physics*, 23(6), 681-684. doi:10.1063/1.1702278
- Collins, R. E. (1976). *Flow of Fluids through Porous Materials*. Tulsa, Oklahoma: Penwell Publishing Co. .
- Cooper, J. W., Wang, X., & Mohanty, K. K. (1999, December). Non-Darcy-Flow Studies in Anisotropic Porous Media. doi:10.2118/57755-PA
- Darcy, H. P. (1856). *Les Fontaines Publiques de la ville de Dijon (The Public Fountains of the City of Dijon (appendix))*. Paris: Victor Dalmont. Retrieved from <https://bae.okstate.edu/faculty-sites/Darcy/>

- Dogulu, Y. S., Venkitaraman, A., Behrmann, L., & Halleck, P. (1995). *Correction of Cross-Diameter Permeability when Measuring over Partial Core Length: Application to API RP 43*.
- Dupuit, J. (1863). *Études Théoriques et Pratiques sur le Mouvement des Eaux (Theoretical and Practical Studies on the Water Movement)*. Paris: Dunod. Retrieved from <https://hdl.handle.net/2027/nyp.33433066341094>
- Evans, E. V., & Evans, R. D. (1988, October). The Influence of an Immobile or Mobile Saturation Upon Non-Darcy Compressible Flow of Real Gases in Propped Fractures (includes associated papers 19901 and 21622 ). doi:10.2118/15066-PA
- Firoozabadi, A., & Katz, D. L. (1979). An Analysis of High-Velocity Gas Flow Through Porous Media. *Journal of Petroleum Technology*. doi:10.2118/6827-PA
- Forchheimer, P. (1901). Wasserbewegung durch Boden (Water Movement Through Ground). *Zeitschrift des Vereines deutscher (Magazine of the German Association of Engineers)*, 45(50), 1781-1788.
- Green, L., & Duwez, P. (1951, March). Fluid Flow Through Porous Metals. *Journal of Applied Mechanics*, 39-45.
- Greenkorn, R. A., Johnson, C. R., & Shallenberger, L. K. (1964, June 1). Directional Permeability of Heterogeneous Anisotropic Porous Media. *Society of Petroleum Engineers*. doi:10.2118/788-PA
- Grove, B., Harvey, J., Zhan, L., & Atwood, D. (2012). An Improved Technique for Interpreting Perforating-Flow-Laboratory Results: Honoring Observed Cleanup Mechanisms. *SPE European Formation Damage Conference*. Noordwijk, the Netherlands: Society of Petroleum Engineers. doi:10.2118/143998-PA
- Halleck, P., Dogulu, Y. S., Behrmann, L., & Venkitaraman, A. (1997, November 1). Correction of Cross-diameter Permeability when Measuring over Partial Core Length: Application to API RP 43. *Journal of Canadian Petroleum Technology*. doi:10.2118/97-11-05
- Haque, M. I. (2015). *Mechanics of Groundwater in Porous Media*. Boca Raton, London, New York: CRC Press Taylor & Francis Group.
- Hubbert, M. K. (1940). The Theory of Ground-Water Motion. *The Journal of Geology*, 48(8), 785-944. Retrieved from <http://www.jstor.org/stable/30057101>
- Hubbert, M. K. (1956). Darcy's Law and the Field Equations of the Flow of Underground Fluids. *Petroleum Transactions*. 207, pp. 222-239. Dijon, France: AIME.
- Johnson, W. E., & Hughes, R. V. (1948, November). Directional Permeability Measurements and their Significance. *Producers Monthly*, 18(1), 17-25.
- Kirchhoff, G. R. (1894). *Vorlesungen über die Theorie der Wärme (Lectures on the Theory of Heat)*. Leipzig: Teubner. Retrieved from [https://archive.thulb.uni-jena.de/hisbest/receive/HisBest\\_cbu\\_00026665](https://archive.thulb.uni-jena.de/hisbest/receive/HisBest_cbu_00026665)

- Klinkenberg, L. J. (1941). The Permeability of Porous Media to Liquids and Gases. *Drilling & Production Practices*, 200.
- Lake, L. W. (1988, April). The Origins of Anisotropy. *Journal of Petroleum Technology*. doi:10.2118/17652-PA
- Liu, X., Civan, F., & Evans, R. D. (1995). Correlation of the Non-Darcy Flow Coefficient. *The Journal of Canadian Petroleum Technology*. doi:10.2118/95-10-05
- Long, J. C., Remer, J. S., Wilson, C. R., & Witherspoon, P. A. (1982, June). Porous Media Equivalents for Networks of Discontinuous Fractures. *Water Resources Research*, 18(3), 645-658.
- Marcus, H. (1962, December). The Permeability of a Sample of an Anisotropic Porous Medium. *Journal of Geophysical Research*, 67(13), 5215-5225.
- Marcus, H., & Evenson, D. E. (1961). *Directional Permeability in Anisotropic Porous Media*. University of California, Berkeley, Water Resources Center Contribution No. 31, Hydraulic Laboratory Uni. of Calif., Berkeley.
- Morita, N. (1974). *Three-Dimensional Permeability Measurement*. Austin, TX: The University of Texas at Austin.
- Morita, N., & Gray, K. E. (1980). Three Dimensional Permeability Measurements. *Society of Petroleum Engineers*. doi:10.2118/9377-MS
- Nye, J. F. (1957). *Physical Properties of Crystals: Their Representation by Tensors and Matrices*. Clarendon Press, Oxford.
- Parsons, R. W. (1964, December). Discussion of Directional Permeability of Heterogeneous Anisotropic Porous Media. *Society of Petroleum Engineers Journal*, 363-364.
- Peters, E. J. (2012). *Advanced Petrophysics - Volume 1*. Austin, TX: Live Oak Book Company.
- Roth, K. (2012). *Soil Physics. Lecture Notes*. Institute of Environmental Physics, Heidelberg University. Retrieved from [www.iup.uni-heidelberg.de/institut/forschung/groups/ts/students/sp](http://www.iup.uni-heidelberg.de/institut/forschung/groups/ts/students/sp)
- Russell, D. G., Goodrich, J. H., Perry, G. E., & Bruskotter, J. F. (1966). Methods for Predicting Gas Well Performance. doi:10.2118/1242-PA
- Scheidegger, A. E. (1954). Directional Permeability of Porous Media to Homogeneous Fluids. *Pure and Applied Geophysics*, 28(1), 75-90.
- Scheidegger, A. E. (1957). *The Physics of Flow Through Porous Media*. University of Toronto Press.
- Siddiqui, F., Soliman, M. Y., House, W., & Ibragimov, A. (2015). Pre-Darcy Flow Revisited under Experimental Investigation. *Journal of Petroleum & Environmental Biotechnology*, 6(6). doi:10.4172/2157-7463.1000249

---

Snow, D. T. (1965). *A Parallel Plate Model of Fractured Permeable Media*. University of California, Berkeley. University of California, Berkeley.

Tariq, S. M. (1990). New, Generalized Criteria for Determining the Level of Underbalance for Obtaining Clean Perforations. *65th Annual Technical Conference and Exhibition*. New Orleans, LA: Society of Petroleum Engineers. doi:10.2118/20636-MS

Walsh, M. P., & Lake, L. W. (2003). *A Generalized Approach to Primary Hydrocarbon Recovery*. Amsterdam Elsevier.

Willhite, G. P. (1986). *Waterflooding*. Richardson, TX: Society of Petroleum Engineers.

You, L., Xue, K., Kang, Y., Liao, Y., & Kong, L. (2013). Pore Structure and Limit Pressure of Gas Slippage Effect in Tight Sandstone. *The Scientific World Journal*, 2013. doi:10.1155/2013/572140

Zeng, Z., & Grigg, R. (2006). A Criterion for Non-Darcy Flow in Porous Media. *Transport in Porous Media*, 63, 57-69. doi:10.1007/s11242-005-2720-3

---

# Product Certification Testing of Perforating System Components

**Justin Erdmann**, *Owen Oil Tools*

Justin is the Test Engineer at Owen Oil Tools, a Core Lab division. He has been with Owen Oil Tools for over 6 years. His primary focus is pressure vessel design and data acquisition systems for pressure and temperature testing. He holds a Bachelor of Science in Mechanical Engineering from the University of Texas at Arlington. Justin also is a registered P.E. in the state of Texas.

**Shaun Geerts**, *Owen Oil Tools*

Shaun has been with Owen Oil Tools, a Core Lab division, since 2012. His experience has been primarily with perforating systems and other ballistic products. He studied at the New Mexico Institute of Mining and Technology earning a Bachelor of Science in Mechanical Engineering, his Master of Science in Mechanical Engineering with Specialization in Explosives Engineering, and a Master of Engineering Management. He currently serves on numerous API subcommittee's, on the committee of IPFC, and as a technical expert for the JIPF.

**James Kinsey**, *Owen Oil Tools*

James has been with Owen Oil Tools, a Core Lab Division, for over 8 years. His experience has been primarily with perforating systems, including limited penetration, consistent hole, and deep penetrating perforating systems. He currently serves as a Project Manager and Lead Shaped Charge Designer in the Energetics Technology Group.

**Jeff Wood**, *Owen Oil Tools*

Jeff has been with Owen Oil Tools, a Core Lab division, for over 12 years. He has experience with most of Owens' product lines including perforating gun hardware, setting tools, bridge plugs, shaped charges, and pipe recovery. Jeff holds a B.S. in Mechanical Engineering from the University of Texas at Arlington. He currently serves as a Project Manager and Design Engineer over perforating gun hardware in the Innovative Technology Group. Jeff also is a registered P.E. in the state of Texas.

---

## Product Certification Testing of Perforating System Components

**J. Erdmann, S. Geerts, J. Kinsey, J. Wood** - Owen Oil Tools

### SUMMARY

The main focus of this paper is to discuss the importance of product and material certification testing of components used in perforating systems. While there are many types of industry accepted test methods, the majority of them are specifically developed for certifying and publishing the performance of a final product. During the depressed Oil & Gas market over the past years it has become critical to find means to reduce costs, but still supply the market with materials that meet existing performance standards. The testing conducted examines the importance of raw explosive powder thermal testing, various types of explosive powder and the effect on performance, and testing of gun steel to ensure the integrity of the perforating gun prior to detonation

### INTRODUCTION

There are many suppliers and manufacturers of perforating system components around the globe. While there are several industry accepted standards or recommended practices for testing perforating system components such as API RP67 and RP19B, many manufacturers have unique internal specifications and standards to which material and products are certified. Over the last several years oil & gas prices have driven the market to become cost competitive. One of the easiest ways to decrease cost is to lower quality: cheaper raw materials, less testing, lower standards of finished goods, etc. However, the market demand dictated an increase in reliability in order to increase field efficiencies and stay profitable.

In addition to a substantial decrease in well completions over several years, when activity increased it created material supply issues for many companies. This created new complications with manufacturers sourcing new and alternate vendors and trying to find suitable substitute materials for their products.

This paper will investigate several of the key components that comprise perforating systems and discuss various tests that were conducted in order to verify and certify the performance of these products. While several of these tests are unique and not an industry standard procedure, it is important to recognize the complexity that goes into providing perforating systems to the market while maintaining a high level of quality and reliability.

The testing conducted includes:

- The effects of PETN detonating cord on performance of Consistent Hole (CH) charges.
- The hole size performance variation between RDX and HMX in CH charges.

- The penetration performance difference between RDX and HMX in Super Deep Penetrating (SDP) charges.
- Temperature effects on sensitivity in alternative binder explosives used in perforators.
- Pressure and temperature testing of gun steel.

Additionally, when examining alternative materials for products, specifically explosives, there is concern with the chemical composition of the binders and the end use of the product application. There has been some research done that shows in Plug & Abandonment operations there can be elevated levels of CO created in the wellbore that can be hazardous during rig operations which can be worsened based on the chemical composition and byproducts of the explosives used (Burky, Craddock, Mason, Rios Osorio, & Harive, 2017). Also the use of fluoropolymers in explosives used to manufacture perforating charges can create noxious gases in misfired perforating guns. The gas generated can create hydrofluoric acid as a byproduct and become concentrated in the perforating carrier when there is a failure to perforate (Potter, 2017).

It is important to recognize that not every product from every company was tested and results may be specific to the product and manufacturer. The results discussed within this paper are not representative of the all perforating products and systems available. The primary reason for this work is to convey the findings from testing and discuss some of the common misconceptions that begin to arise more frequently during the most recent downturn. It is also important to highlight the variability in some products, that appear to meet specifications on paper, but when subjected to actual laboratory testing may not meet the desired performance. All test methods and procedures discussed within this paper follow API RP67 for safe handling of explosives and oilfield equipment (API, 2007).

## TEST METHOD

### *Test Series 1: PETN vs RDX Detonating Cord Performance*

While PETN cord has been a common explosive type used in the industry for decades, it is not typically a recommended product to be used in a majority of perforating gun systems. Instead it is common practice to run RDX cord with RDX charges, HMX cord with HMX charges, etc. A common inquiry during the last several years was, “Is the performance of CH style charges negatively affected when PETN cord is used instead of RDX/HMX Extra High Velocity (XHV) cord?” The main concern is the nominal output velocity of the detonating cords; PETN is 6,400 m/s, while RDX Low Shrink (LS) is 7,000 m/s, and RDX LS XHV is 8,000 m/s.

The first test setup utilized two gun systems fully loaded with charges from the same lot date, the only difference being one gun was loaded with PETN cord and the other was loaded with RDX LS XHV detonating cord. The perforating systems were 3.125” carriers, 6spf-60° phased, and tested fully decentralized in 5.5” 23# P-110 casing. This test only captured the variation in hole size performance. Since these are CH style charges, the penetration was not considered as critical as the hole size. Figure 1 shows the test setup to capture the data in casing. The test would typically show if there was any

potential for interference in the charge performance caused by the reduced velocity from the PETN detonating cord.



**Figure 1: Hole Size Performance Gun Test Setup**

#### *Test Series 2: RDX vs HMX Hole Size Performance Testing*

The next test series conducted was to determine the difference in performance between RDX and HMX. The theoretical maximum detonation velocity of RDX is 8,700 m/s and HMX is 9,100 m/s, resulting in RDX being ~4.5% lower in terms of output velocity. As a result of previous API RP19B test protocols, a majority of Section 1 certified testing has been done with HMX, where a batch size of only 300 charges was required; whereas RDX testing required a batch size of 1,000 charges (API, 2006). It is estimated that 80-85% of perforators made use RDX, but only ~15% of all registered data sheets are for RDX versions of perforating charges. This shows a large discrepancy between the majority of charges being used and the data being published.

Many customers and operators believed that HMX was the preferred explosive for testing because it was a premium explosive and resulted in significantly better performance. During the recent explosive supply issues, HMX supply was starting to become more difficult to keep up with demand. Research showed many operations were running HMX in low temperature wells (where HMX may not be needed) because they believed it was the only way to obtain the published performance. To evaluate this theory a test series of six different gun configurations was conducted, comparing HMX vs. RDX in CH style charges.

For the CH style charge where hole size was of concern, all the charges were loaded into 3.125" diameter perforating carriers of various phasings and shot densities. All the guns were placed in 5.5" 23# P-110 casing, and welded in a fully decentralized orientation with the first shot of the gun being located at the minimum clearance. The test setup, similar to that shown in Figure 1, was lowered into a fluid pit for the test, so the confining fluid was water with no additional cement confinement around the casing string.

#### *Test Series 3: RDX vs HMX Stressed Rock Penetration Performance Testing*

To expand on the above series, Section 2 testing was done on four common SDP charges to confirm penetration performance was also not significantly affected.

It was chosen to use charges specifically designed around deep penetration in high formation strength targets to determine if the penetration performance was negatively affected. The test conditions were tested at a nominal overburden stress state of 5,500 psi and pore pressure of 0 psi. The charges maintained an appropriate setup and air standoff to the respective gun systems, but used a standard 0.75" fluid clearance and 0.5" casing plate as per the new API RP19B Section 2 protocol. The rock used in the test series was a homogenous Berea sandstone with parallel bedding planes. Figure 2 depicts a common Section 2 vessel setup with the key components required for the test. Two tests were

conducted using RDX and two tests using HMX for each charge size as follows: 2.75" (15 gram), 3.125" (21 gram), 3.375" (25 gram), and 4.5" (39 gram).

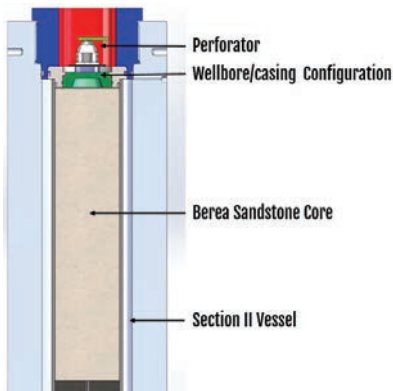


**Figure 2: Section II Test Setup**

#### *Test Series 4: RDX Binder Content Testing*

The fourth test series examined the raw explosive powder itself. As mentioned above, explosive powder supply became scarce during the rapid rise in activity and many alternate sources and suppliers were being considered. A majority of the explosive main load used in the industry is RDX or HMX powder that includes additives such as wax and graphite to help with the manufacturability and decrease the sensitivity of the explosive in the perforators for manufacturing purposes. This content of binder is typically 1-2% by weight for most explosive main loads. There are various types of additives and wax binders that have been used in the industry and in elevated percentages of 3-5% or more.

A concern of the elevated wax/binder contents, as well as the properties of the binder material, is the temperature rating of the binders themselves. Historically the industry has seen negative effects from products like this; when exposed to elevated temperatures for long periods of time the wax/binder was able to melt and desensitize the explosive. Even though the perforating systems did not exceed the temperature ratings of the explosives, the binder rating was insufficient and resulted in significant failures and misruns when ran in the field.

For this test series 3.125" charges were pressed with the new binder content at 5%, five were test for baseline performance and five were tested in a long duration elevated temperature environment. The charges were then placed inside a perforating carrier and loaded inside a heat chamber. The test was conducted at 275°F for 8 hours in order to expose the charges to significant temperatures but not exceed the safe handling limits. Additionally the charges were all orientated with the booster column/initiation point of the charge facing down, this would also be a worst-case scenario where the binder could melt and settle in the booster explosive and cause sensitivity issues. Figure 3 below depicts the test setup of a sacrificial heat vessel being used; the top left graphic is the loaded charge tube, the bottom left shows the loaded perforating carrier and thermocouples, and the right graphic is the test setup.



**Figure 3: Elevated Temperature-Perforator Exposure Test Setup**

After the temperature test, the perforating charges were allowed to cool and then a common industry accepted “playing card gap test” was performed to determine if there was any change in sensitivity. This test places layers of Bicycle® playing cards between the booster column on the perforating charge and the detonating cord requiring the shock to transfer through the cards to initiate the perforator.

*Test Series 5: Gun Steel Testing*

The last test series to be discussed is collapse integrity test of perforating gun carriers under elevated pressure and temperature conditions. Historically it has been witnessed that steel carriers have failed this type of test, even when the raw steel specifications appear to meet industry standards. For this reason when new material suppliers were being sourced and certified to provide raw steel to manufacture gun carriers it was of critical importance to test the material for tensile strength and collapse strength.

For this particular test series the material was tested at 18,750 psi and 400°F for a hold duration of 1 hour once the desired temperature and pressure conditions had been met.

**RESULTS AND DISCUSSION**

*Test Series 1: PETN vs RDX Detonating Cord Performance*

From the two gun tests the hole size was measured in the casing along a standard two axis measurement. The minimum and maximum through hole diameters were recorded, and an average of these two measurements was reported as the average hole size. The data shown in Table 1 are the averaged data of the 12 perforators in each gun; the hole size average decreases by 2% from a 0.42” to 0.41”, and the standard deviation increases from 3.6% to 4.6%.

**Table 1: PETN vs RDX Hole Size Performance**

Detonating Cord Type	Average Hole Size	Standard Deviation
80gr/ft RDX XHV	0.42”	3.6%
80gr/ft PETN	0.41”	4.6%

In addition to measuring the average diameter of the hole size a visual inspection was done on all the perforations to ensure there was no “unusual” perforations that could indicate potential interference in the system. Overall based on the results of the test it did not appear that the

decrease in detonating cord velocity significantly influenced the performance of the system. It is believed the change in standard deviation is within the limits of the perforator itself. There was not a significant change in performance that showed evidence of system interference from the gun system as a result of the lower detonating cord velocity.

*Test Series 2: RDX vs HMX Hole Size Performance Testing*

Based on the 12 perforating gun tests completed, some variations in performance were noted. From Table 2 the lowest difference was 0.2% and the maximum difference was 5.6%, with the average variation of all 70 shots only showing a 2.2% difference in performance. As with the above testing the visual inspection of the casing did not show any concern of variations in hole geometry based on the explosive type used in the perforating charge.

**Table 2: RDX vs HMX Hole Size Performance**

Gun Size	Average Hole Size		
	RDX	HMX	% Diff
18" Gun 3 Shots total	0.36"	0.36"	0.9%
20" Gun 4 Shots total	0.34"	0.32"	5.6%
24" Gun 6 Shots total	0.35"	0.33"	4.6%
24.5" Gun 6 Shots total	0.37"	0.36"	1.1%
26" Gun 7 Shots total	0.36"	0.36"	0.2%
30" Gun 9 Shots total	0.36"	0.35"	0.8%

*Test Series 3: RDX vs HMX Stressed Rock Penetration Performance Testing*

For the Section 2 test series it is more difficult to replicate the test conditions for every test due to the variability in the natural stone and the pressure conditions within the test vessel. Great care was taken to ensure the targets were controlled as closely as possible from their selection and preparation. From the 16 tests examined the average unconfined compressive strength (UCS) was 6,231 psi with a standard deviation of 4.3% and an average target porosity of 19.9% with a 2.3% standard deviation. Additionally during the testing it was recorded that the average overburden stress was 5,494 psi with a standard deviation of 0.8%.

Based on these results it was determined that the test conditions were controlled as well as could be expected given all the parameters of the test method being used. By looking at Table 3, the data being presented is the average of the two RDX tests and two HMX tests of each charge size. The table provides the UCS, porosity of the target when saturated with OMS, and the Total Target Penetration. It appears that RDX and HMX performed similarly in both the 2.75" and 3.125" sizes. However, a difference between RDX and HMX was observed with the 3.375" and 4.5" sizes. The average among all the shots shows the penetration varies by 7.5%. In a full Section II program, a minimum of four shots would be done at a single stress state to obtain a better average performance; only two shots were conducted here for time and cost restraints of the test series. Typically, penetration performance within 10% difference is considered to be within the allowable tolerance of perforating charges. The

difference in performance (between RDX and HMX) for charges below 21 grams was 2.6%, and for charges over 25 grams was 12.5%.

**Table 3: RDX vs HMX Section II Penetration Performance**

Charge Size	RDX Performance			HMX Performance			% Diff
	UCS	Por.	TTP	UCS	Por.	TTP	
2.75"	6200psi	19.54%	13.13"	5768psi	20.47%	13.38"	-1.9%
3.125"	6334psi	19.62%	15.19"	6213psi	19.73%	15.69"	-3.2%
3.375"	6424psi	20.17%	16.69"	6360psi	19.69%	19.56"	-15.9%
4.5"	6622psi	19.90%	16.81"	5930psi	19.73%	18.41"	-9.1%

*Test Series 4: RDX Binder Content Testing*

The perforating charges were placed in a heat chamber with a target temperature of 275°F and a total test duration of 8 hours. Two thermocouples were placed on the tube strip, the first was placed at the end of the tube strip and the second was placed in between 2 charges at the center of the tube length to represent the overall internal gun temperature. Figure 4 shows that the thermocouple attached to the tube strip inside the perforating gun reached 275°F within 2 hours, and the temperature was maintained for an additional 6 hours. The tube strip end temperature is lower than the middle due to the test setup; this was conducted in an open test chamber since it contained explosive materials. The open chamber allowed for minor heat loss at the end of the tube strip, but it was determined to not have a detrimental effect on the test results.

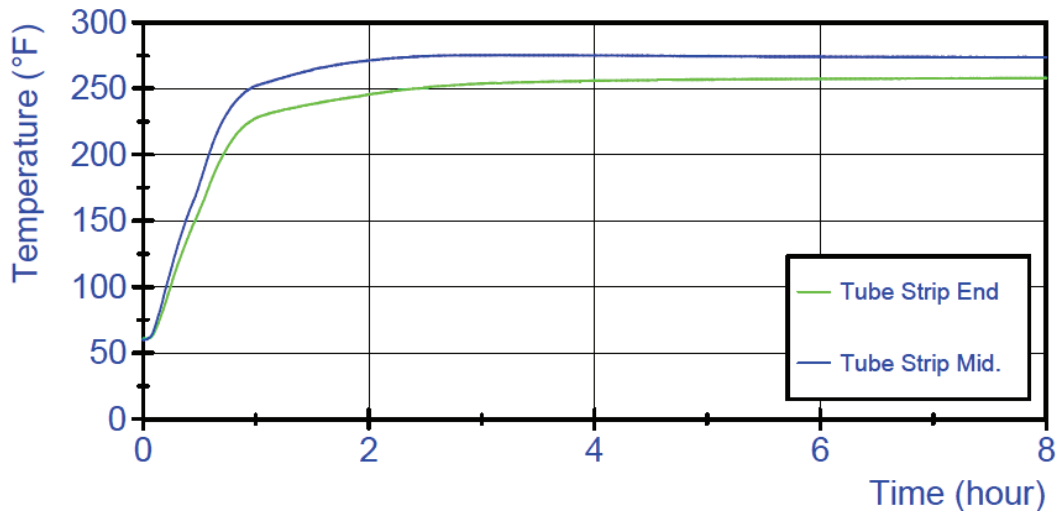


**Figure 4: Temperature Profile of RDX Sensitivity Testing**

From the card gap sensitivity testing results shown in Table 4 the baseline perforators were able to successfully transfer up to 15 playing cards before seeing a failure to initiate. After the charges were removed from the heat chamber it was visually noted that the wax had begun to permeate out of the booster column as well as to the inside cavity of the powdered metal liner. For these heat-cycled charges, the maximum card gap yielding a “pass” result was only 11 cards. This is a ~26% reduction

in sensitivity which confirms the hypothesis that low temperature binders can negatively impact the initiation reliability of the perforating charges when exposed to downhole temperatures.

**Table 4: Temperature Exposed RDX Sensitivity Test Results**

Control		Post Heat	
# Cards	Pass/Fail	# Cards	Pass/Fail
7	Pass	7	Pass
9	Pass	9	Pass
12	Pass	12	Fail
16	Fail	11	Pass
15	Pass	13	Fail

*Test Series 5: Gun Steel Testing*

The carrier for collapse testing was a fully machined, scalloped perforating gun carrier with standard hardware on each end, and fully sealed. The tube strip that typically holds the perforating charges was removed and replaced with a solid aluminum bar that is a smaller diameter than the inner diameter of the carrier. This was done to protect the pressure vessel in case the carrier collapses; the bar allows the carrier to deform, but not fully collapse and potentially be stuck inside the pressure vessel or damage components.

Figure 5 below shows the profile during the test of both temperature and pressure. At the 3.75 hour mark on the test there was an audible “pop” that originated from the pressure vessel and a corresponding drop in pressure was seen. In order to maintain the pressure in the vessel as temperature fluctuates it is common to vent a small amount of pressure to maintain a pressure below the test maximum. This drop was more significant and not due to a drop in pressure that was controlled by the technician running the test, and was later determined to be the gun material yielding and deforming. The pressure was then increased back to the target hold pressure and appeared to remain constant, so the remaining portion of the test was carried out.

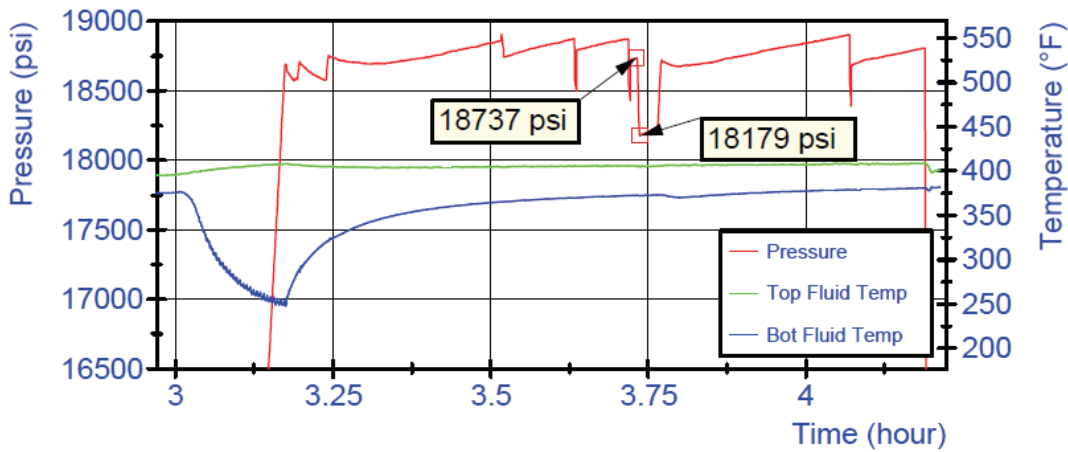


**Figure 5: Temperature and Pressure Profile of Perforating Carrier Testing**

After the test was concluded and the vessel was allowed to cool to a safe temperature the carrier was recovered from the vessel. It was noticeably deformed and measured out of round by  $\pm 0.169''$  on average. The carrier did not fully collapse and maintained the seal of the running hardware, but it was collapsed to the point of being unable to recover the filler bar that had been placed inside the carrier. It was determined that the carrier would have collapsed further if not for the filler bar inside the carrier, so the test was deemed a failure for the material.

## CONCLUSION

Based on the testing results presented within this paper, it was determined that CH perforating charges did not exhibit significantly diminished performance due to the use of PETN detonating cord. The testing also demonstrated that with CH charges in a full system gun test, changing from RDX to HMX resulted in only minor differences in performance. Testing showed an average of 2.2% difference, which is within the expected tolerance of the perforating charges themselves. The Section 2 testing in stressed rock showed that in charges lower than 21 grams, the difference between RDX and HMX was 2.6%; this difference was 12.5% in charges over 25 grams. Being limited to two test per series and having differences in the rock strengths and porosities it is difficult to isolate the performance to only the explosive type.

The elevated temperature testing of components showed several interesting things. The first was that the temperature rating of the binder, if not high enough, could result in melting and desensitization of the perforating charges, increasing the probability of misfires in the perforating system. The second scenario was with elevated pressure and temperature of gun steel; there was mechanical failure in the material.

This paper is not intended to be an exhaustive discussion of all of the testing recommended to certify products used in the perforating industry; rather it is a brief discussion of some of the important characteristics that need to be observed when using new raw materials. What is important to highlight is the critical nature of the specifications and properties of the materials that are used in manufacturing all aspects of perforating products and hardware. It is very difficult to determine performance and how materials will react to the dynamic shock loading caused by explosive detonations without extensive engineering analysis and product testing.

The completions side of the oil & gas industry is required to be extremely efficient and time is one of the most critical factors outside of safety. Market demands, however, can drive expedited product delivery that may sacrifice diligent certification testing leading to failures and misruns that can result in costly lost time and damage depending on the severity. It is important that the products are fully tested and certified by the manufacturer to ensure the final product and all the individual components meet the published performance criteria. While all variables and downhole conditions cannot be replicated in testing, it is critical to conduct thorough product certifications to continue providing high quality products to the meet the evolving market demand.

---

REFERENCES

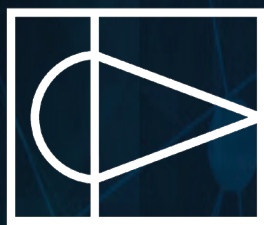
- API. (2006, September). Recommended Practices for Evaluation of Well Perforators. *API Recommended Practice RP-19B*. Washington DC: API.
- API. (2007, May). Recommended Practice for Oilfield Explosives Safety. *API Recommended Practice 67*. Washington DC: API.
- Burky, T., Craddock, G., Mason, J., Rios Osorio, F., & Harive, K. (2017). Carbon Monoxide Hazards from Perforating During Plug and Abandonment Operations. *SPE ATCE* (p. 187036). Houston: SPE.
- Potter, B. (2017). A Brief Study on the Potential Hazards of a Misfired Perforating Gun. *2017 International Perforating Safety Forum* (pp. IPSF 17-08). IPFC.

# JIPF TECHNICAL EDITORS

The Journal of the International Perforating Forum would not be possible without a dedicated network of industry experts to serve as peer reviewers. We gratefully acknowledge the following individuals who have agreed to serve as technical editors for JIPF.

Achim Pabst	DynaEnergetics	Hema Prapoo	AH Wireline
Adam Dyess	Hunting Titan	James Barker	Halliburton
Alex Procyk	Consultant	Jim Gilliat	Baker Hughes
Andrew Werner	Schlumberger	Joern Loehken	DynaEnergetics
Bill Harvey	Baker Hughes	John Carminati	Shell
Bob Haney	Consultant	Lang Zhan	Shell
Brenden Grove	Halliburton	Larry Behrmann	Consultant
Caitlin Bowers	Steel Alloys & Svsc	Lian McNelis	DynaEnergetics
Carlos Bauman	Schlumberger	Mark Brinsden	Shell
Chris Chow	Consultant	Matthew Clay	Owen
Chris Sokolove	Hunting Titan	Meng Yu	Shell
Christian Eitschberger	DynaEnergetics	Niall Fleming	Statoil
Clinton Quattlebaum	Halliburton	Oliver Han	Hunting Titan
Dan Pratt	Owen	Osama Hanna	Consultant
David Cuthill	GEODynamics	Parry Hillis	Baker Hughes
David Underdown	Consultant	Rajani Satti	Baker Hughes
Dennis Baum	LLNL	Ryan White	Baker Hughes
Eliana Mandujano	Imporio Media	Shaun Geerts	Owen
Frank Preiss	DynaEnergetics	Thilo Scharf	DynaEnergetics
Gerald Craddock	Halliburton	Tim LaGrange	Owen

*The executive editors extend special gratitude to Eliana Mandujano. Her vision and creativity continue to be instrumental in producing this top-notch publication; assembling the various content from multiple sources, arranging the overall layout, identifying and incorporating high-quality artwork, and stitching it all together into a seamless professional product.*



**PERFORATORS.ORG**

**INTERNATIONAL PERFORATING FORUM**